CANCER

Targeting VPS18 hampers retromer trafficking of PD-L1 and augments immunotherapy

Ting Dong[1,2]†, Huanmin Niu[1]†, Zhaojun Chu[2]†, Chengjun Zhou[3], Yinghui Gao[2], Mengqi Jia[1], Bin Sun[4], Xiaoxue Zheng[1], Wenru Zhang[2], Jiaozhen Zhang[2], Yanhai Luo[1], Yong Sun[2], Chan Wang[2], Qiqi Lu[1], Changhong Liu[1], Guangfeng Shao[3], Hongxiang Lou[2,5]*, Huiqing Yuan[1]*

Immune checkpoint inhibitors targeting programmed cell death 1 (PD-1) or programmed cell death-ligand 1 (PD-L1) have achieved impressive antitumor clinical outcomes. However, the limited response rates suggest the incomplete understanding of PD-L1 regulation. Here, we demonstrate that vacuole protein sorting 11 and 18 (VPS11/18), two key players in vesicular trafficking, positively regulate PD-L1 and confer resistance to immune checkpoint blockade therapy. VPS11/18 interact with PD-L1 in endosome recycling accompanied by promoting PD-L1 glycosylation and protein stability. VPS18 deficiency enhances antitumor immune response. Pharmacological inhibition by VPS18 inhibitor RDN impaired PD-L1 member trafficking and protein stability. Combination treatment of RDN and anti-cytotoxic T lymphocyte–associated antigen 4 synergistically enhances antitumor efficacy in aggressive and drug-resistant tumors. RDN exerted lung-preferred distribution and good bioavailability, suggesting a favorable drug efficacy. Together, our study links VPS18/11-mediated trans-Golgi network recycling of PD-L1 and points to a promising treatment strategy for the enhancement of antitumor immunity.

INTRODUCTION

Immune checkpoint blockade (ICB) has been the most exciting breakthrough in the treatment of malignant cancers recently (*1*). The cytotoxic T lymphocyte–associated antigen 4 (CTLA-4)/B7 and programmed death 1 (PD-1)/programmed cell death-ligand 1 (PD-L1) are two representative immune checkpoints, which negatively regulate cytotoxic T lymphocyte activity upon T cell activation. Therefore, antibody drugs targeting these two checkpoint-mediated pathways are a successful anticancer strategy in clinics (*2*–*4*). In addition to antibody drugs, small-molecule immune checkpoint inhibitors are also gaining increasing attention because of their pharmacokinetic advantages and obvious therapeutic efficiency (*5*). Although immunotherapy is promising for many cancers, several issues remain to be explored, including how to improve the low or limited response rate for several cancer types, for example, prostate cancer (PCa) and pancreatic cancer, and how to achieve durable responses in patients because one-third of them will relapse over time after therapy (*6*, *7*). Thus, understanding the in-depth mechanisms behind the responsiveness of immunotherapy will shed more light on developing related inhibitors and approaches to markedly improve clinical immunotherapy.

PD-L1 is a major target for immunotherapy, cancer cells often cleverly manipulate it to escape immune surveillance and attenuate ICB efficacy (*2*, *8*). Compelling studies have revealed that PD-L1 expression could be regulated at the transcriptional, translational, and posttranslational levels in cancers (*9*). As a type I transmembrane protein, the trafficking and recycling of PD-L1 have been reported to be crucial in restoring PD-L1 pools and facilitating tumor immune evasion (*10*–*12*). CKLF-like (chemokine-like factor) MARVEL transmembrane domain-containing family member 6 (CMTM6) maintains PD-L1 at the cell membrane and in recycling endosomes, thereby protecting it from lysosomal degradation (*10*). Trafficking protein particle complex subunit 4 (TRAPPC4) interacts with PD-L1 in recycling endoscopes and facilitates its distribution on tumor cell surface regulators via interrupting vesicular trafficking (*13*). Thus, the regulators of PD-L1 emerge as potential therapeutical targets to enhance T cell–mediated antitumor immunity.

Homotypic fusion and vacuolar protein sorting (HOPS) and class C core vacuole/endosome tethering (CORVET) are evolutionarily conserved membrane tethering complexes that play important roles in intracellular trafficking and endosomal sorting (*14*, *15*). Dysregulated expression of subunits of HOPS/CORVET, for example, VPS11 (vacuole protein sorting 11) and VPS18, have been observed in various diseases including cancers (*16*–*18*). In addition to the well-described role in endosomal fusion, VPS18 fine-tunes signaling transductions, including the ubiquitination pathway (*11*, *19*, *20*). As endosomal cycle–related proteins, whether the complex proteins affect membrane proteins, such as PD-L1 internalization, has not been studied. We previously reported that VPS18 conferred multidrug resistance in PCa by promoting lysosome maturation (*21*). Further investigation here reveals that VPS18 and VPS11 act as scaffold proteins for orchestrating trans-Golgi network (TGN) trafficking of PD-L1. VPS18 or VPS11 deficiency impairs PD-L1 retromer trafficking and increases T cell–mediated cytotoxicity. Further attention on VPS18 reveals that the interaction of VPS18 with VPS35, a core member of the retromer complex, results in boosted PD-L1 glycosylation and protein stability. VPS18 inhibition by RDN, a targeting inhibitor we previously identified (*21*), combined with anti–CTLA-4 antibody synergistically enhanced the antitumor efficacy with limited toxicity in murine cancer

[1]Key Laboratory of Natural Products & Chemical Biology of Ministry of Education, Institute of Medical Sciences, The Second Hospital of Shandong University, Jinan, China. [2]Department of Natural Product Chemistry, Key Laboratory of Chemical Biology of Ministry of Education, School of Pharmaceutical Sciences, Shandong University, Jinan 250012, Shandong Province, China. [3]Department of Pathology/Urinary Surgery, The Second Hospital of Shandong University, Jinan, China. [4]National Glycoengineering Research Center, Shandong University, Jinan 250012, China. [5]Traditional Chinese Medicine Department, Shandong Provincial Maternal and Child Health Care Hospital, Jinan, Shandong Province, China.
*Corresponding author. Email: lyuanhq@sdu.edu.cn (H.Y.); louhongxiang@sdu.edu.cn (H.L.)
†These authors contributed equally to this work.

models with metastatic or drug-resistant characteristics, highlighting the importance of VPS18 in antitumor immunity of malignant cancers.

RESULTS

VPS11 and VPS18 are predominant regulators of PD-L1 protein

The CORVET and HOPS complexes are mainly involved in endosomal fusion and sorting for membrane protein trafficking (*14*, *15*), we initially designed in vivo CRISPR screening to determine whether they exert regulatory functions on immune checkpoint proteins and affect ICB therapy. CRISPR screening assays were performed in B16 murine model; single-guide RNA (sgRNA)–transduced B16 cells were transplanted into either $CD8^+$ T cell–depleted mice or immune-competent mice to assess their roles in anticancer immunity (Fig. 1A). The results displayed that, among the targeting candidates, sgRNAs targeting VPS18 and VPS11 were the top ranked, which are negatively enriched in $CD8^+$ cytotoxic T cell (CTL) selection, implicating that targeting VPS11/18 could potentiate cancer cell elimination by CTLs (Fig. 1, B to G). Given the importance of PD-L1 in the antitumor efficiency of ICB therapy, we therefore carried out an in vitro screening based on loss-of-function assays to validate the effect of VPS proteins on PD-L1. The results indicated that VPS18 or VPS11 knockdown markedly diminished PD-L1 expressions, whereas no reduced PD-L1 expressions were observed upon silencing of other core subunits including VPS16 and VPS33A (Fig. 1H and fig. S1, A to C), indicating a specific role of VPS18 and VPS11 in the regulation of PD-L1. This suggests that VPS18 and VPS11 may be functionally related. We also observed that VPS18 or VPS11 depletion, rather than VPS16 or VPS33A, pronouncedly reduced plasma membrane distribution of PD-L1 in docetaxel (Doc)-induced multidrug-resistant PC3/Doc (prostate cancer) and A549/Doc (lung cancer) cancer cells, which were established by Doc exposure and displayed high levels of PD-L1 (Fig. 1I), supporting the specific regulatory effect of VPS18 or VPS11 on PD-L1. Consistent with the transient knockdown results, VPS11 or VPS18 knockout (KO) by CRISPR-Cas9 caused conspicuously down-regulation of PD-L1 in cancer cells (Fig. 1J and fig. S1D). We also demonstrated the effect of knocking down VPS18 in a panel of cancer cell lines (lung cancer cells NCI-460, NCI-H1688, NCI-H292, PCa cells DU145, kidney clear cell carcinoma 786-O, and liver cancer cells HepG2). It was found that the expression of PD-L1 was down-regulated by knocking down VPS18, indicating that the effect of VPS18 on PD-L1 may not be cell line–dependent (fig. S1E).

In the presence of interferon-γ (IFN-γ), induction of PD-L1 by IFN-γ was also abrogated upon VPS11 or VPS18 KO in A549, A549/Doc, and PC3/Doc cells (Fig. 1K and fig. S1, F to H). Furthermore, overexpression of VPS18 or VPS11, instead of VPS16 and VPS33A, sustainedly evokes PD-L1 levels that were stimulated by IFN-γ in PC3 cells (Fig. 1L). The reduced PD-L1 caused by VPS18 depletion was restored in cells when VPS18 or VPS11 was resupplemented, but not when VPS16 and VPS33 were added (Fig. 1, M and N), highlighting the importance of VPS11 and VPS18 in the modulation of PD-L1 that was independent of their roles in HOPS/CORVET complexes. Furthermore, we generated cell lines with double KO of VPS11 and VPS18, revealing a more notable reduction in PD-L1 expression compared to single KO cell lines, suggesting that VPS11 and VPS18 function through the same mechanism (fig. S1I). Of note, interference of VPS11 or VPS18 did not alter the mRNA levels of PD-L1 (fig. S1, J and K), suggesting that this regulation is an mRNA-independent mechanism. Protein half-life analysis indicated that VPS18 deficiency destabilized PD-L1 in the presence of cycloheximide (CHX), a protein synthesis inhibitor (fig. S1L). Overall, these results demonstrated that VPS18 and VPS11 positively regulate PD-L1 protein and membrane distribution in cancer cells.

VPS11 and VPS18 promote PD-L1–mediated suppression on cytotoxic T cell activity

Given that the binding of PD-1 on T cells with PD-L1 in tumor cells compromises T cell–mediated cytotoxicity and confers an immune-suppressive effect (*22*), we sought to assess whether VPS11 and VPS18 affect PD-L1/PD-1–mediated suppression in antitumor immunity. First, we incubated A549 cells with a chimeric protein containing human PD-1 and the Fc fragment of immunoglobulin G (IgG). As measured by flow cytometry, PD-1 binding to tumor cells was markedly impaired upon VPS11 or VPS18 silencing (fig. S2A). Consistently, the results of T cell–mediated killing assays showed that coincubation with activated human peripheral blood mononuclear cells (PBMCs) and tumor cells notably caused an increase in tumor cell apoptosis upon VPS11 or VPS18 depletion, anti–PD-L1 antibody could achieve similar effects as sgVPS11 or sgVPS18 in T cell–mediated killing of A549 cells (fig. S2, B and C). Likewise, cell clone forming assays showed that VPS11 or VPS18 KO markedly reduced the tumor cell survival when coincubated with PBMC, indicating the enhanced anticancer effect of cytotoxic T cells (fig. S2D). To dissect the role of VPS11 and VPS18 in ICB therapy in vivo, we established VPS11 or VPS18 stable KO Lewis lung carcinoma (LLC) cells and then established subcutaneous tumor models (Fig. 2A). The results clearly showed that VPS18 or VPS11 silencing substantially improved animal survival and inhibited tumor growth in the presence of $CD8^+$ T cells (Fig. 2, B and C). In line with the reduced tumor burden, ex vivo analysis revealed that VPS18/11 KO tumors impaired PD-L1 expression (Fig. 2D and fig. S2E), accompanied by increased percentages of $CD3^+$ $CD8^+$ T cells, $CD8^+$ $CD69^+$ T cells, and $CD8^+$ $CD107a^+$ in the tumors (Fig. 2E). Furthermore, the tumor-infiltrating $CD8^+$ T cells in the VPS11/18 KO tumors had an increased effector function compared to those from the parental tumors, evidenced by their capacities to secrete granzyme B (GzmB) and IFN-γ (Fig. 2F). Collectively, these results indicate that VPS11/18 are simulators of tumor growth, which is associated with the suppression in T cell–mediated immunity. We choose VPS18 to further investigate whether the effect of VPS18 on tumor growth directly influences ICB therapy. Drug-resistant murine PCa RM1/Doc cells ($VPS18^{high}$) and their paired RM1 cells were used to establish the tumor model in C57BL/6 mice (fig. S2F). The results indicated that VPS18 silencing (RM1/Doc-shVPS18) notably inhibits tumor growth, whereas overexpression of VPS18 in RM1 cells (RM1-VPS18) notedly promoted tumor growth (fig. S2, G to I). VPS18 knockdown evidently increased the antitumor response of drug-resistant tumors to anti–PD-1 therapy, but overexpression of VPS18 caused resistance to this therapy (fig. S2, G to I). Analysis of T cell infiltration in tumor tissues revealed that $CD8^+$ T cells were slightly increased in samples from the mice harboring RM1/Doc-shVPS18 and became notably evident in mice treated with anti–PD-1 antibody (fig. S2J). By contrast, decreased $CD8^+$ T cells were obviously in RM1-VPS18 tumors, this inhibition was not restored in tumor

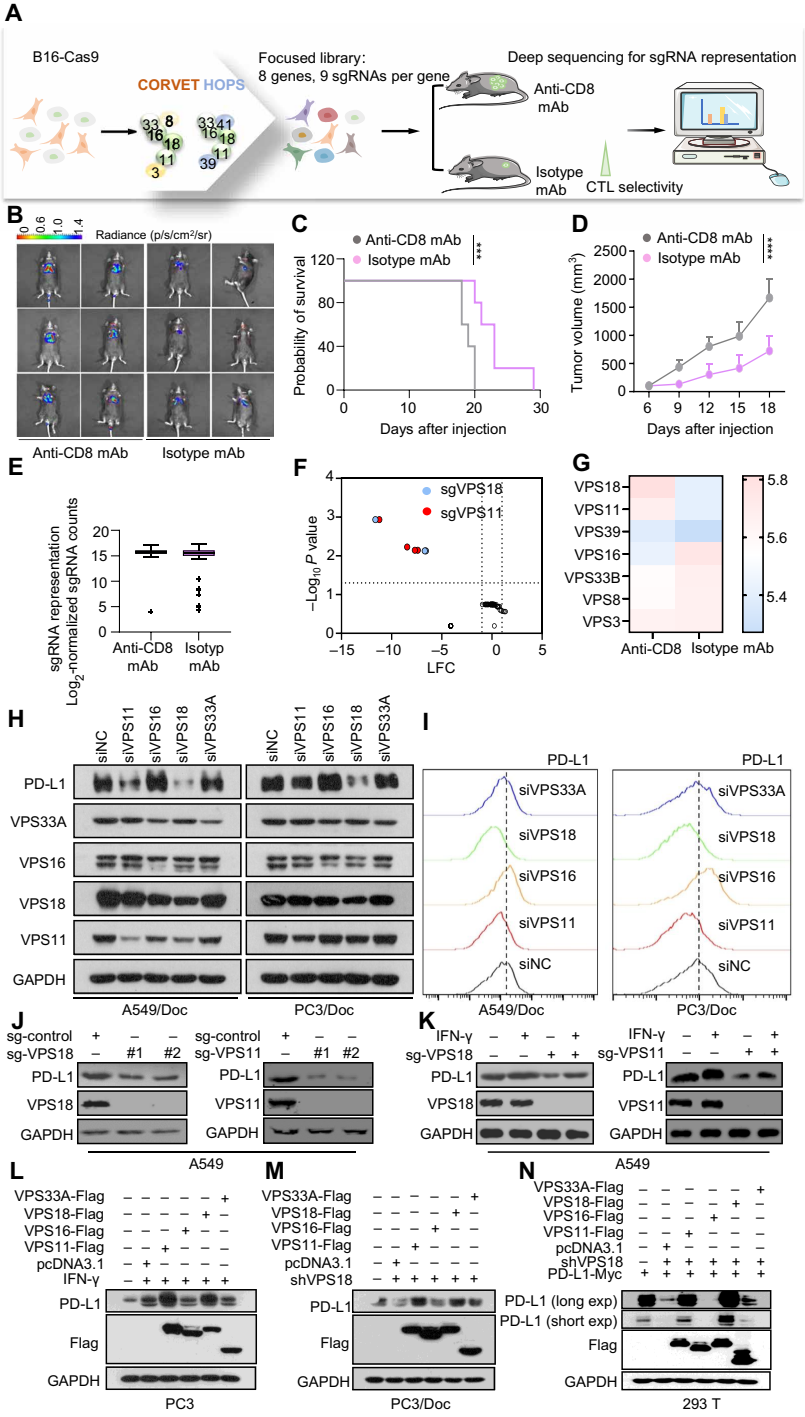

Fig. 1. VPS11 and VPS18 are a predominant regulator of PD-L1 protein. (**A**) Schematic diagram of the in vivo focused screens in the B16 mouse melanoma cell line expressing luciferase (B16-luc). (**B**) Representative whole-body bioluminescence images of mice. C57 mice were subcutaneously injected with B16 cells, followed by 200 μg of anti-CD8 monoclonal antibody (mAb) and 200 μg of isotype mAb on days 0, 3, 6, 9, and 12, respectively. Day 0 is the tumor induction day ($n = 6$). (**C** and **D**) Quantification of Kaplan-Meier survival curves (C) and tumor volumes (D) of C57 mice treated with anti-CD8 mAb and isotype mAb ($n = 6$). (**E**) sgRNA representation in C57 mice treated with anti-CD8 mAb and isotype mAb. (**F**) Scatter plots showing the in vivo CTL selectivity of each targeted gene. (**G**) Heatmap showing expression differences of VPS family. (**H**) Western blot showing PD-L1 expression in PC3/Doc and A549/Doc cells transfected with small interfering RNAs targeting different VPS complex subunits. (**I**) Flow cytometry showing the cell surface expression of PD-L1. (**J**) Western blot showing PD-L1 protein levels in VPS11 KO or VPS18 KO A549 cells. (**K**) Western blot showing the effect of VPS11 or VPS18 depletion on interferon-γ (IFN-γ)–induced PD-L1 expression. (**L**) Western blot showing the expression of PD-L1 in PC3 cells transfected with different VPS complex subunits and treated with a combination of IFN-γ. (**M**) Western blot showing PD-L1 expression in VPS18 knockdown cells cotransfected with each subunit of VPS-Flag plasmids. (**N**) Short hairpin RNA knockdown of VPS18 in 293 T was cotransfected with PD-L1–Myc and each subunit of VPS-Flag plasmids and subjected to analysis of the expression of PD-L1 by Western blot. GAPDH, glyceraldehyde-3-phosphate dehydrogenase.

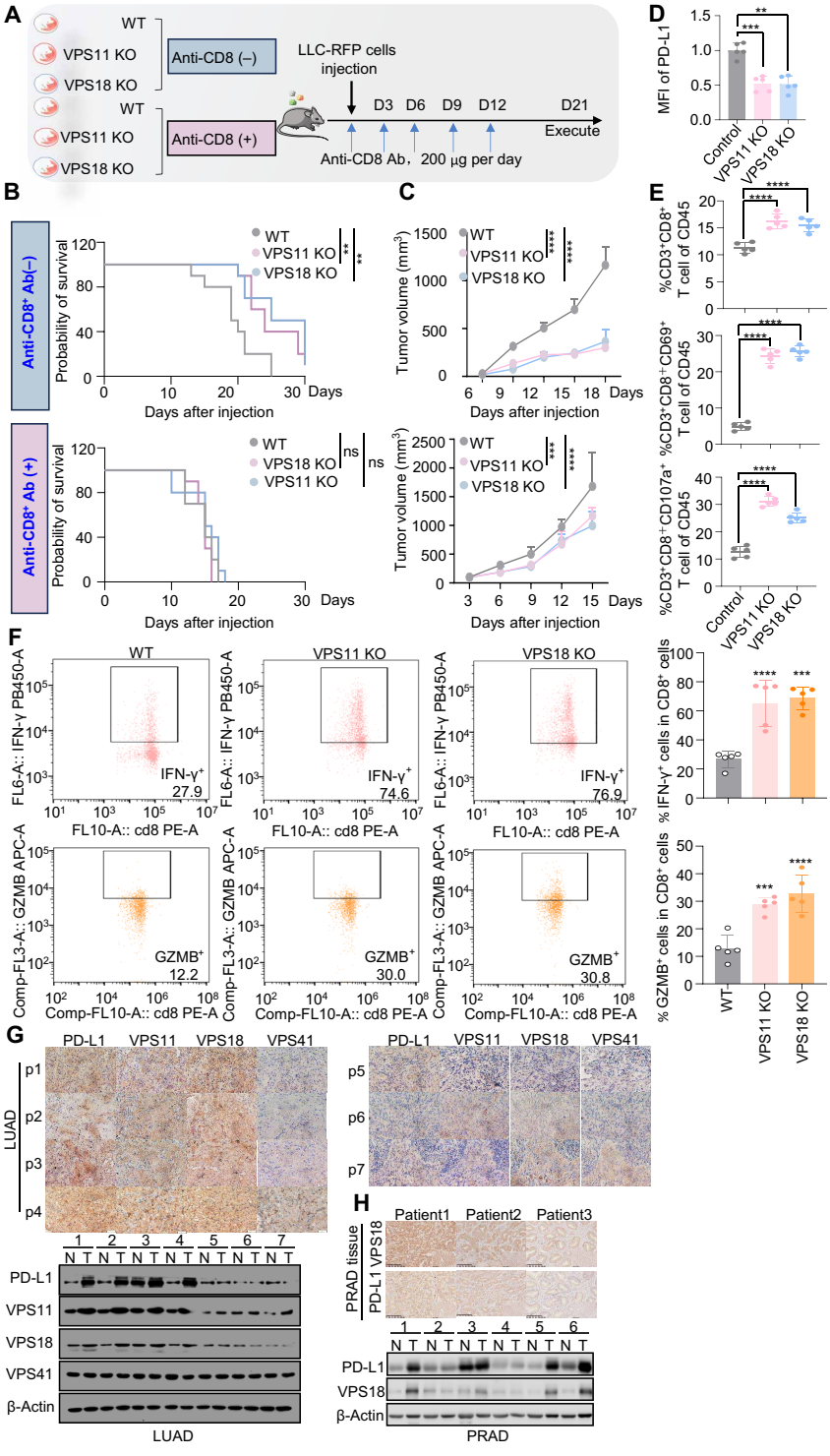

Fig. 2. VPS11 and VPS18 promote PD-L1–mediated suppression of cytotoxic T cell activity. (**A**) VPS11 KO, VPS18 KO, and WT LLC-RFP cells were injected into C57BL/6 mice with or without CD8 antibody (200 μg per day on days 0, 3, 6, 9, and 12). (**B** and **C**) Quantification of the probability of survival (B) and tumor volume (C) of immunocompetent or $CD8^+$ T cell–depleted mice injected with LLC-RFP cells as described in Fig. 3D. $n = 10$ in (B) and $n = 5$ in (C). (**D**) PD-L1 expression on cell surface detected by flow cytometry ($n = 5$). (**E**) Flow cytometry showing the activation and function of tumor-infiltrating T cells. ($n = 5$). (**F**) Representative dot plots (left) and quantifications (right) of the proportions of IFN-γ and granzyme B (GzmB) expressing tumor-infiltrating $CD8^+$ T cells ($n = 5$). (**G** and **H**) Immunohistochemical staining in human lung adenocarcinoma (LUAD) (G) and prostate adenocarcinoma (PRAD) samples (H). Scale bars, 50 μm ($P = 3.8 \times 10^{-9}$). Western blot showing the levels of indicated proteins in the normal (N) and tumor (T) tissues. ns, no significance.

samples exposed to PD-1 antibody if compared with the control groups (fig. S2J). The cytotoxic activity of T cells was validated by GzmB expressions and IFN-γ production in RM1/Doc-shVPS18 tumors and was more potent in tumors treated with PD-1 antibody when compared with the control groups, but this change pattern was noticeably impaired in RM1-VPS18 tumors (fig. S2, K and L). We also explored the clinical relevance of the mechanism behind VPS/PD-L1 that would be potent predictors for guiding ICB therapy; clinical lung adenocarcinoma and prostate adenocarcinoma samples were analyzed for this purpose. As shown in Fig. 2 (G and H), VPS18 and VPS11 expressions were positively correlated with PD-L1 abundance. To increase the sample size of the experiment, lung adenocarcinoma tissue chips were purchased for further evaluation. The immunofluorescent staining results showed a positive association between VPS18 and PD-L1 expression (fig. S2M). Together, VPS11 and VPS18 suppress T cell–mediated antitumor immunity, which is ascribed to the regulatory effect on PD-L1.

VPS18 and VPS11 physically interact with PD-L1 via their RING domains

Given that VPS11 and VPS18 were implicated in stabilizing PD-L1 protein, independent of the VPS complex, we test the possibility that VPS11- or VPS18-mediated stability of PD-L1 is a consequence of their direct interactions. The results of coimmunoprecipitation (co-IP) assays revealed that endogenous PD-L1 noticeably interacted with VPS18 and VPS11, but not VPS16 and VPS33A in cancer cells (Fig. 3A and fig. S3A). Upon depleting VPS11 or VPS18 in A549 cells, the interaction between VPS18 or VPS11 and PD-L1 was detected to remain intact (fig. S3A); reciprocally, the binding activity of VPS11 to PD-L1 was also observed in the absence of VPS18. Similarly, the interactions between VPS11 and VPS18 with PD-L1 were confirmed when we introduced plasmids expressing Myc-labeled PD-L1 and Flag-labeled VPS11/18/16/33A into 293 T cells, whereas deleting the cytoplasmic tail of PD-L1 abolishes this interaction (Fig. 3B and fig. S3, B and C). Immunofluorescence staining analysis clearly showed that endogenous VPS11 or VPS18 was well colocalized with PD-L1 in A549 and PC3 cells (Fig. 3, C and D). Since both VPS18 and VPS11 encompass a RING domain with E3 ubiquitin ligase activity at the C terminus (*18*), which is not present in VPS16 and VPS33A, we generated deletion mutants of VPS18 and VPS11 lacking the RING domains (VPS18-ΔRING and VPS11-ΔRING) to examine the involvement of the RING domain in PD-L1 regulation. Deleting of the RING domain in VPS18 or VPS11 ablated their ability to stabilize PD-L1 (Fig. 3E) and failed to interact with PD-L1 (Fig. 3F and fig. S3D), implicating a crucial role of the RING domain in the regulation of PD-L1. Considering the RING domain has E3 ubiquitin ligase activity that is required for protein ubiquitination and degradation, we therefore determined the effect of VPS18 or VPS11 on PD-L1 ubiquitination. However, overexpression of VPS18 or VPS11 yielded limited changes in the PD-L1 ubiquitination (fig. S3E). Overall, the RING domain of VPS11/18 and the C cytoplasmic tail of PD-L1 are essential for the interaction between VPS11/18 and PD-L1.

To check whether the above interaction is dependent on VPS11-VPS18 complex formation, recombinant proteins of VPS11-HA and VPS18-Flag or VPS18$^{\Delta N}$-Flag were incubated for 1 hour to facilitate the complex formation, and then added PD-L1 protein for the subsequent co-IP experiment. Results show that VPS11 interacts with VPS18 but not VPS18$^{\Delta N}$, which is consistent with the previous reports that N terminus is required for VPS11-VPS18 interaction (fig. S3F) (*23*, *24*). However, PD-L1 could interact with VPS11 regardless of the presence or absence of the VPS18 N-terminal domain (fig. S3G). Upon introducing either VPS18, VPS18$^{\Delta N}$, or VPS18$^{\Delta Ring}$ into PC3 cells, we observed that both VPS18 and VPS18$^{\Delta N}$ overexpression, but not VPS18$^{\Delta Ring}$, were capable of enhancing PD-L1 expression (Fig. 3G), suggesting that loss of the N-terminal domain in VPS18, which resulted in disruption of VPS11/VPS18 complex formation, is still able to up-regulate PD-L1 in the presence of VPS11. These results support that the formation of the VPS11-VPS18 complex is dispensable for PD-L1 regulation. Together, VPS18 and VPS11 interact with PD-L1 by the RING domain that is not triggered for PD-L1 ubiquitination degradation.

VPS11/18 maintain PD-L1 glycosylation and protein stability via TGN recycling endosomes

Dynamic transportation between endocytic recycling compartments and lysosome-mediated degradation systems affects the stability and expression of PD-L1 (*10*–*13*). As vacuolar trafficking proteins, we explore whether VPS11/18 participates in PD-L1 recycling via recycling endosomal carriers (RAB-dependent), or retrograde transport pathway from late endosome/TGN to the plasma membrane (*25*). We initially investigated whether RAB4 and RAB11, two major proteins in recycling endosomes, can regulate PD-L1. While silencing of RAB4A, to some extent, increased PD-L1 levels, RAB11A knockdown resulted in a reduction in PD-L1 (Fig. 4A), suggesting that RAB11A, but not RAB4A, contributed to PD-L1 endosomal recycling transport in drug-resistant cells. PD-L1 protein rapidly dropped down when RAB11A was down-regulated in cells exposed to CHX, supporting the involvement of RAB11A in PD-L1 stability (fig. S4A), consistent with the report that RAB11-positive recycling endosomes act as a restoring pool of PD-L1 (*13*). We performed co-IP experiments to question the association of VPS18 and RAB11A. The results displayed that RAB11A was obviously detected in the silver-stained gel that was precipitated by the VPS18 antibody, hinting at the interactions between these two proteins (Fig 4B). We exogenously expressed VPS11/18 and PD-L1 in 293 T cells to confirm these interactions, VPS18, VPS11, and PD-L1 were notedly observed in immunocomplexes precipitated by HA-RAB11A (Fig. 4C and fig. S4B). The images of immunofluorescence assays indicated colocalization of PD-L1 in RAB11-marked recycling endosomes was evident in control cells, associated with an intact membrane distribution of PD-L1 (Fig. 4D and fig. S4C). However, silencing of VPS11 or VPS18 led to considerably reduced PD-L1 fluorescence in RAB11-recycling endosomes, overexpression of VPS18 rescued PD-L1 abundance and colocalization with RAB11 endosomes (Fig. 4D and fig. S4C).

In addition to the recycling of PD-L1 to the plasma membrane, glycosylated modification of PD-L1 which usually occurs in the Golgi is essential for its stability on the membrane (*26*–*28*). We stepped further to explore whether VPS11/18-facilitated PD-L1 recycling requires glycosylation through a TGN-mediated retrograde pathway. To specifically clarify their roles in PD-L1 trafficking, we turned to the classic immunoadsorption method to probe the effect of VPS11or VPS18 on the cellular localization of PD-L1 (*29*). A substantial amount of PD-L1 was immunoabsorbed with TGN-46, syntaxin-6, which are enriched in the TGN, whereas less PD-L1 was co-adsorbed with TGN-46 in VPS11 or VPS18 KO cells (Fig. 4E).

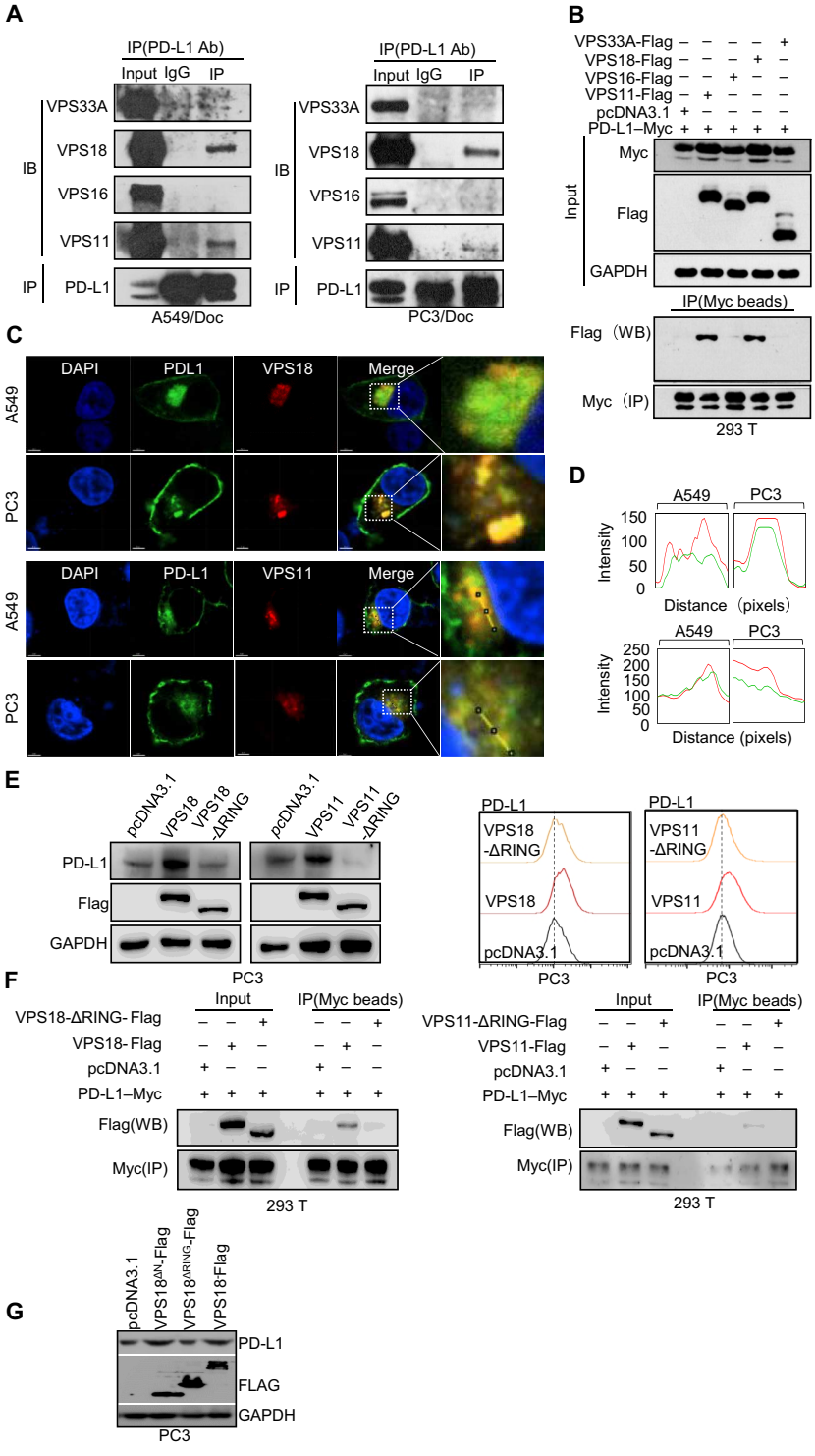

Fig. 3. VPS18 and VPS11 physically interact with PD-L1 via their RING domains. (**A**) Co-IP assay indicating the interaction between endogenously expressed PD-L1 with VPS18 and VPS11 in A549/Doc and PC3/Doc cells. (**B**) 293 T cells were cotransfected with PD-L1–Myc, and each subunit of VPS-Flag plasmids and subjected to IP for Myc beads. (**C**) Representative immunofluorescence images showing both PD-L1 (green) and VPS18 (red) or VPS11 (red) localized in recycling endosomes in A549 and PC3 cells. Scale bars, 5 μm. (**D**) The fluorescence intensity profiles of VPS18/11 and PD-L1 along the yellow line in (C). This experiment was repeated three times independently with similar results. (**E**) Western blot and flow cytometry analysis of the expression of PD-L1 in PC3 cells transfected with VPS18-Flag or mutants lacking RING domain (VPS18-ΔRING-Flag) plasmids. (**F**) Co-IP for detecting the interaction between PD-L1–Myc with VPS18-Flag, VPS18-ΔRING-Flag, VPS11-Flag, and VPS11-ΔRING-Flag. (**G**) Western blot analysis of the expression of PD-L1 in PC3 cells transfected with VPS18-Flag or mutants lacking N domain ($VPS18^{\Delta N}$-Flag) or RING domain ($VPS18^{\Delta RING}$-Flag) plasmids.

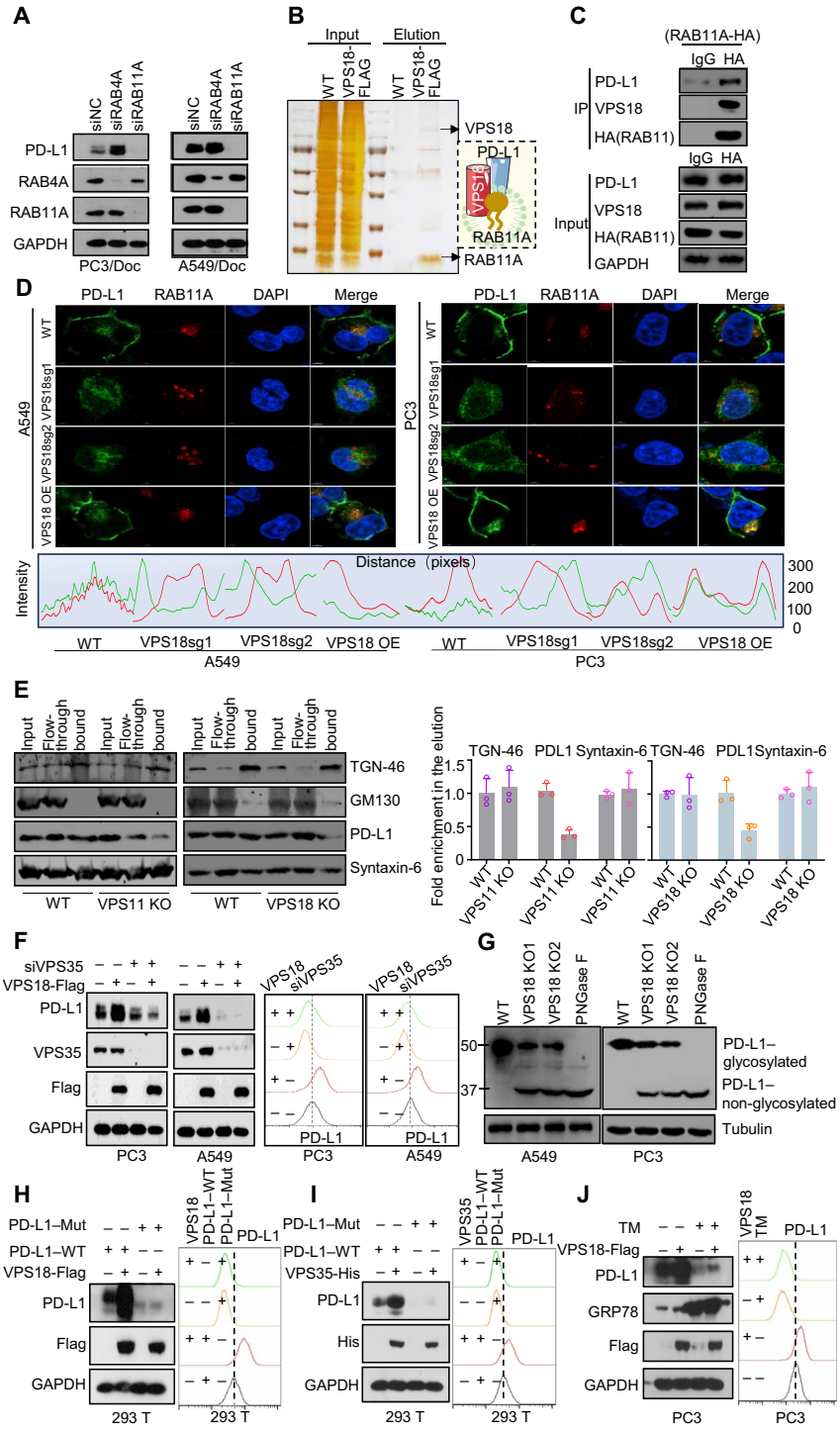

Fig. 4. VPS11/18 maintain PD-L1 glycosylation and protein stability via TGN recycling endosomes. (**A**) Western blot showing PD-L1 expression in PC3/Doc or A549/Doc cells transfected with siRAB4A or siRAB11A. (**B**) Silver staining showed the existence of RAB11A in VPS18 immunoprecipitation. (**C**) Co-IP assays showing the interaction among RAB11A, PD-L1, and VPS18. (**D**) Representative immunofluorescence images of PD-L1 (green) and recycling endosome (RAB11A, red) in the indicated cell lines. The intensity profiles of RAB11A and PD-L1 along the yellow line were plotted on the bottom panels. Scale bars, 5 μm. (**E**) Immunoblot of TGN-46 immunoadsorption from wild-type (WT) and VPS11 KO or VPS18 KO A549 cells. TGN-46 membranes were immunoisolated using anti–TGN-46 antibody in the absence of detergent. The input, unbound flow through, and elution were run on SDS–polyacrylamide gel electrophoresis and blotted for TGN markers syntaxin-6, cis-Golgi marker GM130, and PD-L1. Right: Quantification of Western blot. (**F**) VPS18 overexpression was performed in combination with VPS35 knockdown, and the expression of PD-L1 was analyzed by Western blot and flow cytometry. (**G**) Western blot showing PD-L1 levels in WT, VPS18 KO1, VPS18 KO2, and peptide *N*-glycosidase F–treated cells. (**H** and **I**) Western blot and flow cytometry analysis of the expression of PD-L1 in PD-L1–WT or PD-L1–Mut overexpression in combination with VPS18 (H) or VPS35 (I) overexpression. (**J**) Western blot and flow cytometry analysis of the expression of PD-L1 in VPS18 (N) or VPS35.

Besides TGN-46, vacuolar protein sorting 35 (VPS35) is also a well-documented protein because of its role in intracellular protein transport (*30*, *31*). The results demonstrated that VPS35 depletion notably suppressed PD-L1 abundance and protein stability in various cell lines (Fig. 4F and fig. S4, D and E). Furthermore, we depleted VPS18 in VPS35 KO cells and observed that the expression of PD-L1 was not further decreased compared to when either VPS18 or VPS35 alone was absent (fig. S4F). Similar results were observed in cells silencing VPS11 and VPS35 (fig. S4F). In addition, supplementation of VPS18 or VPS11 could not restore PD-L1 expression in VPS35 knockdown PC3 or A549 cells (Fig. 4F and fig. S4G), suggesting that the regulatory effect of VPS11 and VPS18 on PD-L1 was dependent on VPS35 and shared the same mechanism behind PD-L1 regulation. The associations among PD-L1, VPS18/11, and VPS35 were further validated by endogenous and exogenous co-IP assays and immune-fluorescence imaging (fig. S4, H to J). Therefore, VPS11/18 promote the PD-L1 trafficking, at least in part, through endosome recycling and Golgi-network retrograde transport pathways.

Considering that the activity of PD-L1 is tightly regulated by *N*-glycosylation, we are investigating whether Golgi residency of PD-L1 affects PD-L1 glycosylation. Our data indicated that glycosylation of PD-L1 (~45 kDa) was inhibited when loss of VPS18/11 and sharply dropped down in the presence of PNGase (peptide *N*-glycosidase) which is an enzyme to hydrolyze glycosides. Notably, glycosylation of PD-L1 gradually reduced its stability upon VPS11/18 depletion, supporting the role of VPS11 and VPS18 in mediating TGN recycling to sustain PD-L1 stability (Fig. 4G and fig. S4K). To validate that VPS18-mediated TGN transport of PD-L1 maintains PD-L1 glycosylation, we generated point mutation plasmids of PD-L1 at N35, N192, N200, and N219 [asparagine (N) to glutamine (Q), termed "PD-L1–Mut"] (fig. S4L), which are essential for PD-L1 glycosylation (*26*). As the ability of TGN-46 on protein glycosylation has been elucidated previously (*32*), we try to explore the involvement of VPS35 in VPS18-mediated regulatory effect on PD-L1 glycosylation. It was clearly shown that VPS18 and VPS35 enhanced PD-L1 levels and membrane distribution; however, mutant PD-L1 (PD-L1–Mut) markedly caused a reduction in PD-L1 protein, but not mRNA, and lost its ability to sustain on plasma membrane even though VPS18 or VPS35 was overexpressed in cells (Fig. 4, H and I, and fig. S4M). Furthermore, PD-L1 glycosylation was obviously suppressed in response to tunicamycin (TM), a glycosylation inhibitor, leading to the disappearance of PD-L1 on the cell membrane. Notably, glycosylated PD-L1 was partially restored when VPS18 or VPS35 overexpressed in cells exposed to TM (Fig. 4J and fig. S4N), supporting the importance of retromer complexes in VPS18-mediated PD-L1 recycling and glycosylation. Collectively, these findings demonstrate that enhancement in PD-L1 glycosylation is ascribed to, at least partially, the association of VPS11/18 with TGN recycling endosomes, leading to increased protein stability and cell surface location (fig. S4O).

RDN manipulates PD-L1 endosomal trafficking and enhances T cells toxicity by targeting VPS18

Given the importance of VPS in PD-L1 regulation, we conducted a screening of in-house compounds, particularly the compounds targeting various VPS subunits that were intentionally included, to monitor the changes in PD-L1 secretion by cell-based enzyme-linked immunosorbent assay (ELISA) assays. The chemical information is described in table S1. Screening results revealed that RDN, an aminomethylated derivative of bisbibenzyl riccardin D, previously identified as a VPS18 inhibitor by our group (*11*), was the most potent compound that notably down-regulate PD-L1 expression (fig. S5A), at a concentration without cellular cytotoxicity (fig. S5B). Thus, RDN was selected to examine whether it can regulate PD-L1 and affect ICB therapy. RDN predominantly reduced PD-L1 abundance and membrane levels in a time- and dose-dependent manner with or without IFN-γ induction in multiple cancer cell lines (Fig. 5A and fig. S5, C to E); this inhibition exacerbated the abolishment of PD-L1 in cells treated with CHX (Fig. 5B). Overexpression of VPS18 notably rescued PD-L1 levels and membrane presence that was markedly suppressed by RDN in cancer cells (Fig. 5, C and D). We also assessed the effect of RDN on PD-L1 endosome trafficking. The results indicated that RDN treatment notably impaired the localization of PD-L1 on the cell surface and RAB11A-positive endosomes, indicating that RDN suppressed PD-L1 endosome trafficking and protein maintenance (Fig. 5, E and F). Also, RDN interrupted the refreshing of PD-L1 glycosylation and transport by the TGN pathway as evidenced by the changes in co-adsorbed PD-L1 and TGN-46 and glycosylated PD-L1 levels (Fig. 5G and fig. S5, F to J).

Next, we evaluated the effect of RDN on T cell–mediated toxicity due to its inhibition of PD-L1.

Lung cancer cells A549 and phytohemagglutinin (PHA) induced Jurkat T cells or activated PBMC cells were cocultured upon RDN treatment, and surviving tumor cells were visualized by Real-Time Cellular Analysis (RTCA). As shown in Fig. 5 (H and I), RDN reduced cancer survival; this effect was boosted when cancer cells were cocultured with Jurkat T cells, suggesting the involvement of T cells in RDN-enhanced cellular toxicity. In contrast, overexpression of VPS18 in cancer cells impaired T cell triggered cellular toxicity and attenuated the effect of RDN (Fig. 5I). Together, RDN enhances the cytotoxicity of T cells toward cancer cells by suppressing PD-L1 stability and trafficking.

Lung-specific homing of RDN inhibits lung cancer growth in mice

Drug off-targeting and/or no selected distribution in organs not only causes adverse effects but also determines inadequate efficacy in the clinic (*33*). Thus, we went a further step to estimate the pharmacokinetic characteristics of RDN before evaluating its tumor-suppressive effect. Quantitative analysis of RDN was conducted on the various tissues from RDN-treated mice using imaging mass spectrometry that can determine the spatial distribution and quantify drug metabolites in tissue sections. Obviously, RDN was predominantly distributed in the lung tissues when compared to the liver, kidney, heart, and spleen and appeared to be pretty low in the brain (Fig. 6, A and B). The results of concentration-time profiles among these tissues revealed that RDN reached the maximal concentration at 8 hours after injection and then declined until almost disappeared on day 6 (fig. S6A), providing better dosage guidance for therapy in vivo. Moreover, we plotted the plasma level and time curve to monitor the changes of RDN after injection by liquid chromatography–tandem mass spectrometry (LC-MS/MS; fig. S6B). The plasma concentration of RDN in mice immediately decreased after injection and remained until day 6 (fig. S6C). Thus, the pharmacodynamic study indicates that RDN has a long half-life and exerts a favorable distribution in the lung.

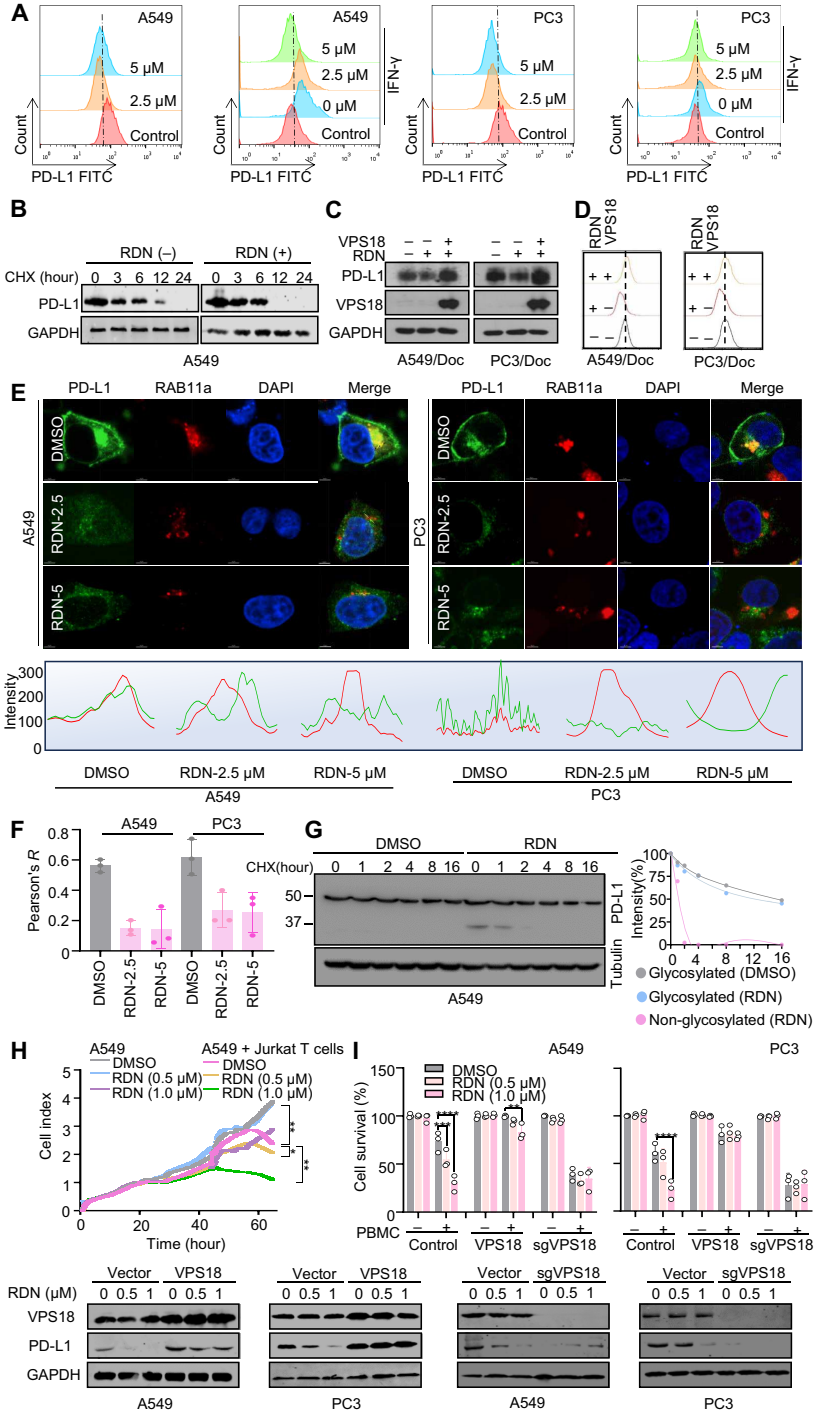

Fig. 5. RDN manipulates PD-L1 endosomal trafficking and enhances T cell toxicity by targeting VPS18. (**A**) Changes in PD-L1 levels in IFN-γ–stimulated cells (100 ng/ml, 24 hours) with indicated concentrations of RDN treatment for 6 hours were detected by flow cytometry ($n = 3$). (**B**) Western blot analysis of PD-L1 levels in A549 cells treated with both 2.5 μM of RDN for 24 hours and 20 mM CHX at indicated intervals ($n = 3$). (**C** and **D**) Cells overexpressing VPS18 were treated with a combination of RDN (5 μM) for 6 hours and the expression of PD-L1 was analyzed by Western blot (C) or flow cytometry (D). (**E** and **F**) Representative immunofluorescence images of PD-L1 (green) and RAB11a (red) in A549 (left) and PC3 (right) cells treated with 2.5 or 5 μM of RDN for 6 hours. The intensity profiles of RAB11 and PD-L1 along the yellow line were plotted on the bottom panels. (**G**) Western blot analysis and quantitative analysis of PD-L1 levels in A549 cells. Cells were treated with 20 mM CHX at indicated intervals along with 2.5 μM of RDN or dimethyl sulfoxide (DMSO) treatment for 24 hours. (**H**) Cell impedance assay of activated Jurkat T cells toward cancer cell killing. Following a 24-hour treatment with the specified RDN concentration (0.5 or 1.0 μM), Jurkat T cells [stimulated by phytohemagglutinin (PHA; 1 μg/ml), 48 hours] were introduced in a 1:3 ratio for 48 hours. The xCELLigence system (Agilent) with RTCA Software was used to conduct a real-time analysis of the results ($n = 3$ biological replicates). Statistical significance was determined by a two-sided, unpaired *t* test. $^{**}P < 0.01$. (**I**) Cell survival analysis and Western blot analysis of VPS18- and sgVPS18-transfected A549 and PC3 cells with the treatment of RDN (0.5 or 1.0 μM) for 48 hours ($n = 3$).

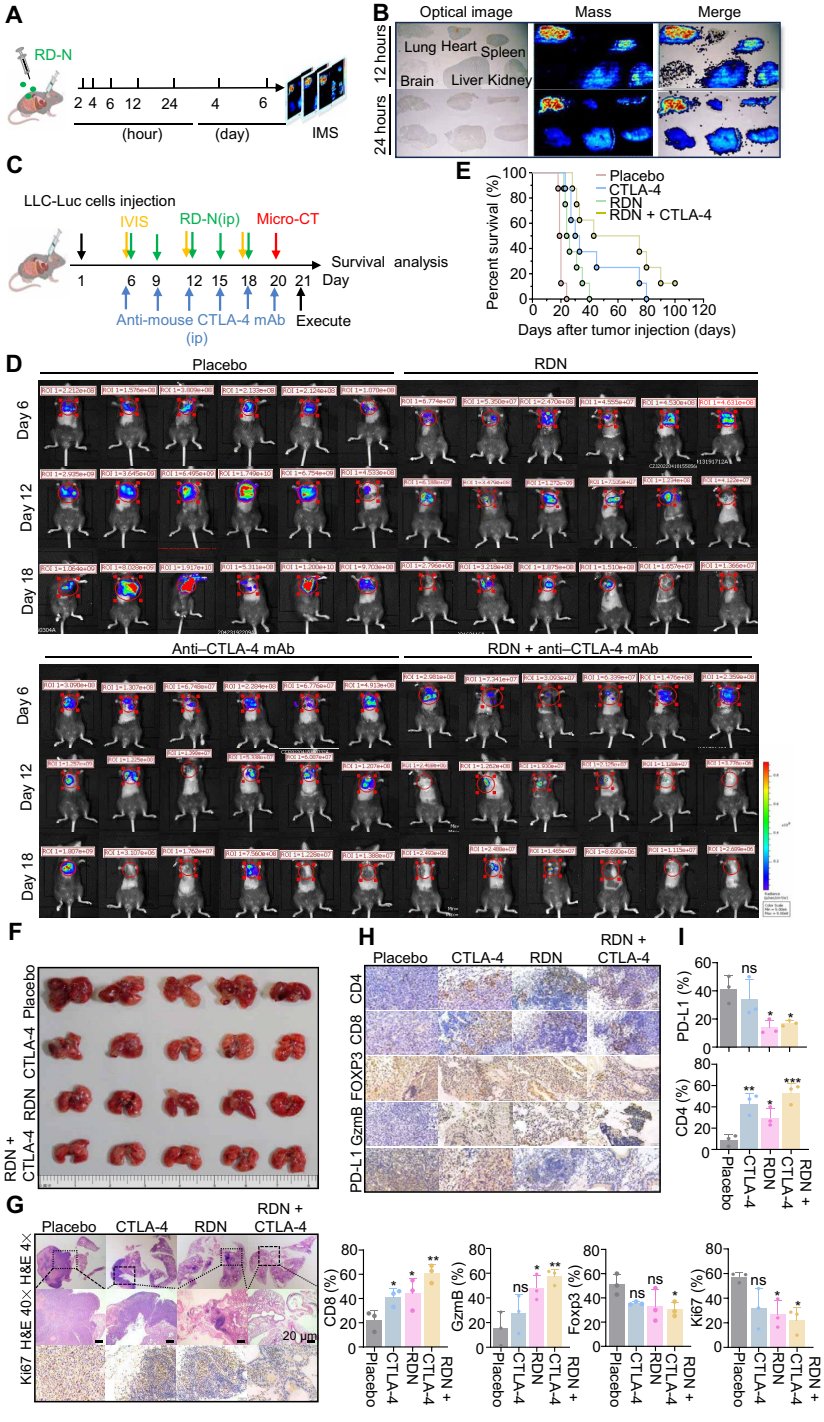

Fig. 6. Lung-specific homing of RDN inhibits lung cancer growth in mice. (**A**) Flowchart of tissue distribution of RDN in C57BL/6 mice detected by mass spectrometry imaging. (**B**) Representative mass spectrometry image of the distribution of RDN in the tissue at 12 and 24 hours after RDN (20 mg/kg) was injected into the tail vein. The red-green-blue (RGB) image was generated by "MIRION," which was converted from the original file after setting a unified threshold. (**C**) Flowchart of pharmacodynamic study of RDN combined with anti–CTLA-4 in the lung of C57BL/6 mice to construct an in-situ model of lung cancer. C57BL/6 mice were randomly divided into the model group, RDN (10 mg/kg), RDN (10 mg/kg) combined with the anti–CTLA-4 group (100 μg), and the anti–CTLA-4 group (100 μg). Each group consisted of 14 mice, 6 for pharmacodynamic evaluation and 8 for survival analysis. (**D**) Analyzed fluorescence signals using an in vivo imaging instrument (PerkinElmer) in mice levels ($n = 6$). (**E**) Survival analysis of mice in each group ($n = 8$). (**F**) Anatomical map of lung tissue of each group of mice ($n = 5$). (**G**) Hematoxylin and eosin (H&E) staining of lung tissue of each group of mice. Scale bars, 200 μm. Immunohistochemistry (IHC) staining displays Ki67 expression of lung tissue of each group. Scale bars, 20 μm. ($n = 6$). (**H**) IHC staining displays CD4, CD8, FOXP3, GzmB, and PD-L1 expressions of lung tissue from each group. Representative images of six biologically independent samples. Scale bar, 200 μm. (**I**) Quantitative results of IHC staining for CD4, CD8, Foxp3, Ki67, GzmB, and PD-L1 (relative to placebo). Data are means ± SD, $n = 3$. Statistical significance was determined by a two-sided, unpaired t test. $^*P < 0.05$, $^{**}P < 0.01$, and $^{***}P < 0.001$.

Given the inhibitory effect of RDN on PD-L1 and lung preferable distribution, we explored whether RDN could achieve notable therapeutic effects against lung cancer in combination with anti–CTLA-4 antibodies, a feasible combined strategy with enhanced efficacy and acceptable adverse events in the clinic. To this end, LLC cells were implanted into the lung of C57BL/6 mice to establish an orthotopic lung cancer model treated with RDN alone or RDN plus anti–CTLA-4 antibody (Fig. 6C). Either RDN or anti–CTLA-4 antibody alone was able to inhibit tumor growth; mice treated with a combination of RDN and anti–CTLA-4 showed marked improvement in survival and elimination of the lung tumor (Fig. 6, D to G, and fig. S6, D to H). In addition, combined treatment was associated with acceptable adverse effects, as we did not observe impaired morphologic changes in other tissues (fig. S6G). The alterations of immune responsive parameters were further analyzed in the treated mice model. Besides down-regulated PD-L1 levels, the combination treatment resulted in pronounced augmentation of tumor-infiltrating $CD4^+$ and $CD8^+$ T cells in tumor samples companied with an increase in GzmB, as well as decreased Foxp3 (T_{regs}, which possessed immunosuppressive functionality), indicating an enhanced immunity response (Fig. 6, H to I, and fig. S6H). These cumulative results demonstrated a potential role of RDN in synergizing with anti–CTLA-4 immunotherapy through modulation of the immune microenvironment.

RDN sensitizes CTLA-4 blockade therapy for metastatic or drug-resistant tumors in mice

As the efficiency of combination treatment in situ tumor models, we extended our study to further examine the effect of RDN on metastatic tumors. The murine B16 melanoma is one of the most widely used metastatic tumor models in anticancer therapy studies (*34*). B16-luc cells were delivered to C57BL/6 mice by tail vein injection and randomly divided into eight groups with RDN or combined with anti–CTLA-4 treatment; RDN was subjected to mice with low, medium, and high concentrations, respectively (Fig. 7A). The results of body weight monitoring were consistent with our observations that RDN had limited effect on body weight of the treated mice (fig. S7A). Bioluminescence tomography clearly showed that the combination therapy with RDN and CTLA-4–targeting antibody effectively suppressed the lung metastasis of tumors over the time course; the low dosage of RDN displayed effectiveness and became more potent with increased concentrations (Fig. 7, B and C). Consistently, the lung tissues displayed a notable reduction of melanoma metastatic lesions in the combined treatment groups as indicated by a reduced number of tumor nodes in the lung (Fig. 7, D to F). Collectively, the mice receiving the combined therapy exhibited a notable synergistic advantage and inhibition of the metastasis of melanoma cells to the lung, suggesting the combination administration of RDN and anti–CTLA-4 may be a potential treatment for aggressive tumor in the lungs.

We were inspired to explore the possibility of whether RDN is also effective in tumors with a low response to ICB therapy, for example, PCa. Androgen-independent and invasive murine PCa cells RM1 have been subjected to Doc to establish multidrug-resistant cells (RM1/Doc) where VPS18 is highly induced. The results clearly indicated that tumor growth was marginally inhibited upon CTLA-4 inhibitor treatment alone; however, RDN predominantly augmented anti–CTLA-4 efficacy in mice bearing RM1/Doc cells, as indicated by minimal residual tumor size, tumor weight, and $CD8^+$ T cells (Fig. 7, G to I, and fig. S7B), with no substantial changes in body weight (fig. S7C) and functions of the liver and kidney (fig. S7, D and E). While hydroxychloroquine (HCQ), a targeting inhibitor of lysosomes has been reported to sensitize immunotherapy in pancreatic cancer by degrading major histocompatibility complex I (*14*), it showed notable suppression of tumor growth when combined with anti–CTLA-4 antibody but with less efficacy when compared to cotreatment of RDN and CTLA-4 inhibitor (Fig. 7, G to I). In addition, HCQ treatment caused a detectable reduction in body weight and increased toxicity in the liver and kidney (fig. S7, D and E). We further examined the intratumoral immunocytes upon various treatments. The tumor-infiltrated $CD8^+$ T cells and their activity (GzmB positivity staining) were evident in mice treated with RDN alone and further augmented by cotreatment with CTLA-4 inhibitor, displaying better effects than that of HCQ combination treatment (Fig. 7, J and K). Meanwhile, treatment with RDN, but not HCQ, was associated with a reduction of PD-L1 in tumors (fig. S7F). Together, targeting VPS18 by RDN offers an option for aggressive and drug-resistant tumors that benefit from ICB immunotherapy when co-treatment with CTLA-4 inhibitor.

DISCUSSION

This study identified VPS18 and VPS11 as critical regulators to stabilize PD-L1 protein and explored the mechanism of VPS18 in regulating retromer-mediated trafficking of PD-L1. Glycosylation via VPS18-VPS35–mediated retromer cycle facilitated PD-L1 stability and membrane location, which led to immunotherapy resistance. Thus, targeting VPS18 by a small molecular compound RDN pronouncedly sensitized drug-resistant cancer cells to CTLA-4 blockade and reversal immunotherapy resistance.

Anti–PD-1/PD-L1 therapy is the cornerstone of current immunotherapy, which has provided substantial clinical benefits in multiple malignancies (*35*). Therefore, understanding the regulatory mechanism of PD-L1 is critical to guide the clinical application of PD-1/PD-L1 inhibitors. As a transmembrane protein, the trafficking of PD-L1 in recycling endosome or endosome/lysosome pathway determines its activity and the efficacy of immunotherapy, receiving more attention for this regulation (*9*). For example, the cell membrane presence of CMTM6 and CMTM4 directly interacts with PD-L1 and inhibits its endocytosis and degradation (*10*). Using haploid genetic screening data in this article, we also found that VPS11 and VPS18 are the potential regulators of PD-L1, like CMTM6 and CMTM4 (*10*). TRAPPC4 promotes RAB11-mediated recycling of PD-L1 (*13*). Huntingtin-interacting protein 1–related protein, one of the important components of the endocytic machinery, acts as a negative regulator to deliver PD-L1 lysosomal degradation (*11*). Our results identify regulatory factors (VPS11/VPS18/VPS35) and intracellular trafficking pathways (endosome-Golgi network) in PD-L1 regulation. Beyond being subunits of the VPS complexes, VPS18 or VPS11 acts as a scaffold to interact with PD-L1 and VPS35 retromer, promoting retromer-mediated recycling of PD-L1 to Golgi. VPS18/VPS35-mediated retromer cycling of PD-L1 refreshes PD-L1 glycosylation and facilitates its distribution on the cell surface. Depletion of VPS18 by short hairpin RNA (shRNA) or pharmaceutical inhibition of VPS18 by RDN (a small-molecule agent targeting VPS18) notably suppresses PD-L1, leading to notable increases in T cell–mediated cytotoxicity in vivo. Ritter *et al.* (*36*) reported that the ESCRT complex composed of

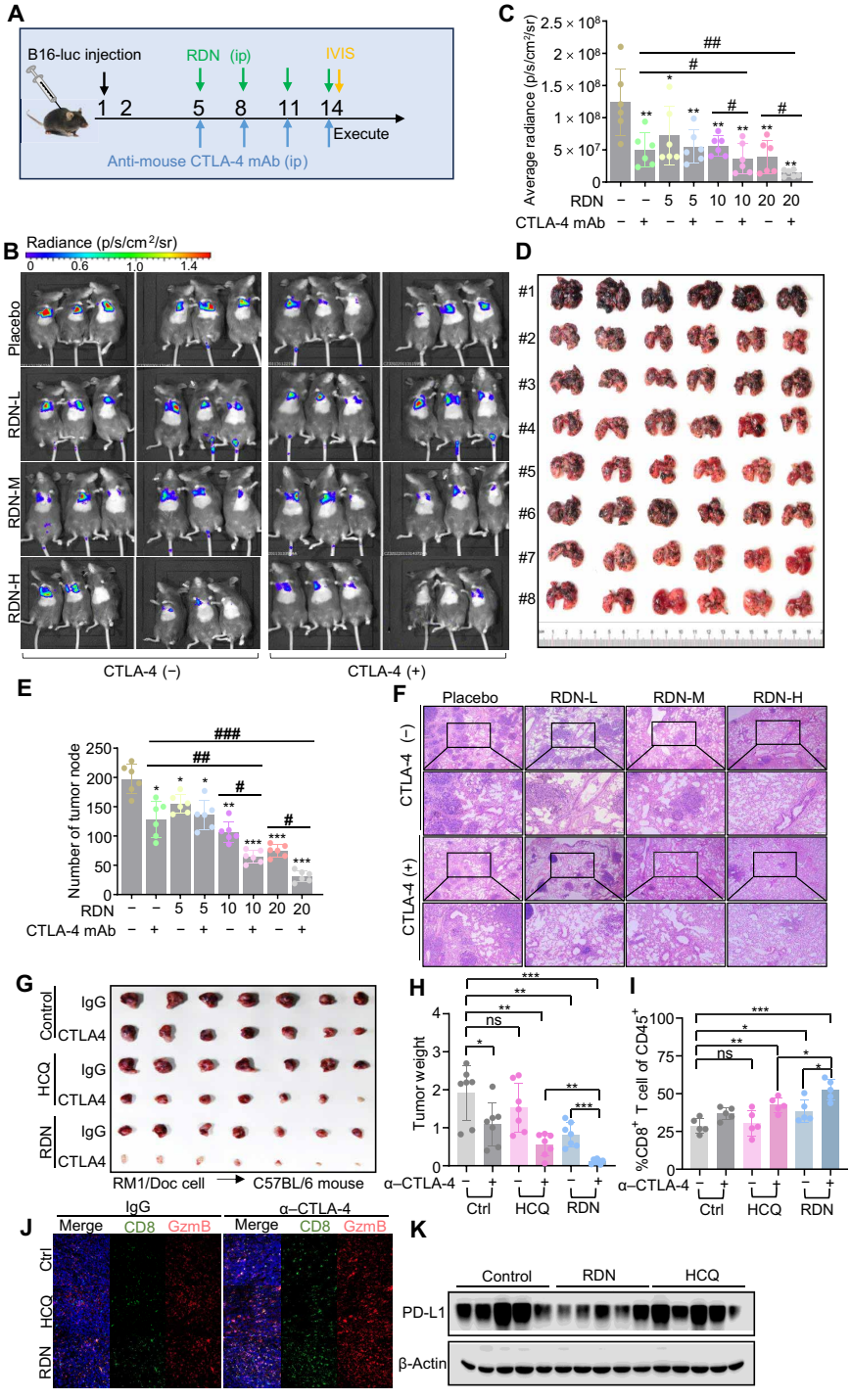

Fig. 7. RDN sensitizes CTLA-4 blockade therapy for metastatic or drug-resistant tumors in mice. (**A**) Flowchart of pharmacodynamic study of RDN combined with anti–CTLA-4 in lung metastasis model of melanoma. Then, they were randomly divided into the model group, the RDN group (5, 10, and 20 mg/kg), RDN (5, 10, and 20 mg/kg) combined with the anti–CTLA-4 group (200 μg), and the anti–CTLA-4 group (200 μg) ($n = 6$). (**B** and **C**) In vivo images and quantitative statistical results of fluorescence intensity of small mice in each group. Data are means ± SD, $n = 6$. Statistical significance was determined by a two-sided, unpaired t test. $^{*}P < 0.05$ and $^{**}P < 0.01$ (relative to #1); $\#P < 0.05$ and $\#\#P < 0.01$. (**D** and **E**) Anatomical map of lung tissue and statistical results of melanoma nodule count in each group of mice. ($n = 6$). #1 (Vehicle), #2 (CTLA4), #3 (RDN 5 mg/kg), #4 (RDN 10 mg/kg), #5 (RDN 20 mg/kg), #6 (RDN 5 mg/kg+CTLA4), #7 (RDN 10 mg/kg+CTLA4), #8 (RDN 20 mg/kg+CTLA4). Data are means ± SD, $n = 6$. Statistical significance was determined by a two-sided, unpaired t test. $^{*}P < 0.05$, $^{**}P < 0.01$, and $^{***}P < 0.001$ (relative to #1); $\#P < 0.05$, $\#\#P < 0.01$, and $\#\#\#P < 0.001$. (**F**) H&E staining results of lung tissue of mice in each group. Scale bars, 200 μm. Representative images of six biologically independent samples. (**G** to **I**) Statistical analysis of the images of tumors (G), tumor weight (H), and the percentages of $CD3^{+}$ $CD8^{+}$ T cells (I) ($n = 7$). (**J**) The expression of CD8 and GzmB was detected by immunofluorescence in each group. (**K**) The total expression of PD-L1 was detected by Western blot in RDN and the hydroxychloroquine (HCQ) group.

several VPS proteins, which exhibit sorting of endocytosed cargo for degradation, is involved in antitumor immunity by participating in cell membrane repair. These results suggest that VPS proteins may contribute to immune response through different mechanisms. VPS18 and VPS11 have been found to modulate estrogen receptor α signal transduction as E3 ubiquitin ligases in breast cancer independent of the VPS complex (*20*). However, our data demonstrated that E3 ligase domains of VPS18 and VPS11 were required for binding to PD-L1 with no ubiquitin-dependent digestion. Meanwhile, except for VPS11/VPS18/VPS35, which positively regulate the expression of PD-L1, we also found that VPS16 was able to negatively regulate PD-L1. We speculate that the negative regulatory effect of VPS16 on PD-L1 was due to its competitive combination with the RING domain of VPS18 and VPS11 (*16*). These findings reveal that VPS subunits exert additional functions by themselves, even though they are subunits of a complex such as VPS18 and VPS16 in the VPS complex, beyond mediating endosomal fusion, lysosomal maturation in a complex-depend manner. Further investigations are needed to uncover the functions of the RING domains of VPS18 and VPS11 in the regulation of PD-L1 and interpret how VPS16 suppresses PD-L1.

As components of the HOPS/CORVET complexes, VPS11 and VPS18 functionally cross-talked with VPS35, a component of the retromer complex, collaboratively promoting PD-L1 membrane presentation. VPS35 is reported to increase the proliferation of hepatic cancer cells through sorting and trafficking of transmembrane receptor fibroblast growth factor receptor 3 (*30*). It appears that protein-protein interactions among VPS members or association with others are crucial in determining their functions. Future studies are expected to discover if VPS18/VPS35 interactions influence other transmembrane proteins. In this study, our results clearly indicated that combination treatment with RDN, a small-molecule inhibitor targeting VPS18, and anti–CTLA-4 antibody predominantly enhanced the antitumor efficacy with little toxicity in drug-resistant PCa cells, one of the "cold" malignant tumors (*37*). These results not only provide solid evidence that VPS18 is critical in the regulation of immune response but also synergistically improve the outcome in cancers that have a pretty low response for immunotherapy. Overall, our study demonstrates that the interactions of VPS18/VPS35 promote retromer trafficking of PD-L1 and suggest that targeting VPS18 paves a promising way to improve benefits for combined immunotherapy.

MATERIALS AND METHODS

Antibodies and reagents

Derivatives of natural products (tables S1) were synthesized by our research group at the Institute of Natural Pharmaceutical Chemistry, Shandong University. Ki67 Rabbit pAb antibody, GzmB Rabbit pAb antibody, CD86 Rabbit pAb antibody, and CD56 Rabbit pAb antibody were purchased from ABclonal Technology Co., Ltd. CD4 antibody, CD8 antibody, and Foxp3 antibody were purchased from Servicebio Technology Co., Ltd. The InVivoMAb anti-mouse CTLA-4 antibody was purchased from Bio X Cell Co., Ltd.

Patient samples

PCa tissue chip was purchased from Shanghai Outdo Biotech Company (HProA150PG02). PCa and lung cancer tissue samples were obtained from surgical excision specimens at the Second Hospital of Shandong University. Utilization of the clinical samples was approved by the Ethical Committee of Shandong University [KYLL-2021(KJ)P-0276].

Cell lines

PCa PC3 cells and Doc-resistant PC3/Doc cells, murine RM1 and Doc-resistant RM1/Doc PCa cells, lung cancer A549 cells, Doc-resistant A549/Doc cells, Jurkat (E6–1) cells, and murine melanoma B16-luc cells were cultured in RPMI 1640 medium. Murine Lewis cells (LLC, LLC-Luc, and LL2-RFP) were cultured in Dulbecco's modified Eagle's medium (DMEM) supplemented with 10% fetal bovine serum (HyClone) and penicillin (100 U/ml) and streptomycin (100 g/ml). LLC (CS0098) cells were purchased from Beijing Ding Guo Technology Co., Ltd. (Beijing, China). LLC-Luc (LZQ0009) cells were purchased from Shanghai Zhong Qiao Xin Zhou Biotechnology Co., Ltd. LL2-RFP cells were stored in our laboratory. 293 T cells were cultured in DMEM. All these cells were routinely cultured in 5% CO_2 at 37°C. After chemical treatments, cells were collected for Western blot or other assays. Dimethyl sulfoxide was used as the vehicle control.

Animal

All animal experiments were approved by the Ethics Committee of Shandong University [KYLL-2021(KJ)A-0070]. C57BL/6 mice (6-week-old male) were purchased from the Animal Center of the China Academy of Medical Sciences (Beijing, China). Female SD rats were procured from Beijing Vital River Laboratory Animal Technology Co., Ltd. (Beijing, China).

Transfection

The lentiviral-based shRNA used to knock down expression of human VPS18 was purchased from Hanbio Biotechnology (Shanghai, China). The lentiviral-based shRNA used to knockdown or overexpression of mouse VPS18 was purchased from Genomeditech Biotechnology (Shanghai, China). Then, we constructed stable cells of VPS18 for subsequent experiments according to the manufacturer's instructions. For RNA interference, small interfering RNA (siRNA) duplex oligonucleotides or scramble oligonucleotides were synthesized from GenePharma (Shanghai, China). In total, 100 pmol of siRNA was added in one well from a six-well plate. About 48 to 72 hours after the transfection, the cells were harvested for further analysis The siRNA sequences are provided in table S2.

Plasmids

The full-length VPS18 and truncated VPS18 plasmids (VPS18-ΔRING) were provided by Y. Kawaoka (University of Tokyo). VPS11, VPS16, VPS33A, VPS35, and PD-L1 plasmids were purchased from ViGene Biosciences (Jinan, China). VPS11-ΔRING and PD-L1–Mut plasmids were constructed by Abiotech (Jinan, China). For the transfection of plasmids, we used the jetPRIME Transfection Reagent (Polyplus transfection). Cells were harvested ~48 hours after transfection for further analysis.

For Flag-tagged PD-L1 and hemagglutinin (HA)-tagged VPS11, VPS18, and RAB11 constructs, PD-L1, VPS11, VPS18, and RAB11 genes were amplified using A549 cDNA as a template and inserted into pcDNA3.1-3XFlag or pcDNA3.1-3XHA plasmid. Deletion mutants of the N domain of VPS18 ($VPS18^{\Delta N}$) were generated by isolating by polymerase chain reaction (PCR) the regions of the open reading frames (ORFs) corresponding to amino acids 350 to 973 for VPS18 and inserting them into expression vector pcDNA3.1(+).

VPS11/18 knockout A549 cell lines

CRISPR-Cas9 KO of VPS18 and VPS11 in A549 cells were generated as previously described (*25*). Briefly, firstly, sgRNA sequences were cloned into pLenti CRISPR V2. For the production of lentiCRISPR viruses, 293 T cells were seeded 1×10^5 cells into six-well cell culture plates before transfection. The DNA mixture consisted of lentiCRISPR-v2, psPAX2, and pMD2.G plasmids was incubated with jetOPTIMUS DNA transfection reagent (Polyplus) at room temperature for 20 min and then added to 293 T cells. The lentivirus-containing supernatant was collected at 24 and 48 hours and stored at −80°C. For lentiviral transfection, 1×10^4 A549 cells were seeded into a 12-well plate. The next day, cells were transduced with lentiviruses using polybrene (10 μg/ml). Cells were selected with puromycin for 72 hours. KO efficiency was tested at the protein level by immunoblotting. sgRNA sequences are as follows: sgVPS11-1: TTTCTTACAGGTTTCACAGA; sgVPS11-2: GGCAGTGTTACATTGAACAA; sgVPS18-1: AGGGTATGTGAATGCCCAGC; sgVPS18-2: GGGCACTTCCTTCTCCAGCT.

Western blot analysis and immunoprecipitation

Cells were washed with ice-cold phosphate-buffered saline (PBS) and lysed in radioimmunoprecipitation assay (RIPA) lysis buffer with protease inhibitors and phosphatase inhibitors (Invitrogen). Protein concentrations were quantified by BCA protein assay (Beyotime). Western blot analysis was performed using standard techniques. Blots were incubated with primary antibodies overnight at 4°C before being probed with the appropriate peroxide-conjugated secondary antibodies. The immunocomplexes were captured by the addition of 20 μl of Protein A/G PLUS-Agarose beads (Santa Cruz Biotechnology) and washed three times with RIPA wash buffer. After recovery by heating at 95°C for 5 min in 30 μl eluent with 0.1 M glycine (pH 3.0) twice; samples were neutralized by 1 M tris-HCl of pH 8.5. After mixed with 4× SDS loading buffer, the immunocomplexes were analyzed by Western blotting. The detailed antibody information is included in table S1.

Real-time quantitative PCR

Total RNA was extracted from cultured cells using an RNAiso plus kit (TaKaRa) according to the manufacturer's instructions. Real-time PCR was performed with SYBR Green. The primers used to amplify target genes are listed in table S3.

Immunofluorescence

Cells growing on glass coverslips were washed thrice with PBS, then fixed with ice-cold methanol/acetone (1:1) for 5 min, and incubated with 3% bovine serum albumin (BSA) for 30 min. Following washing with PBS containing 0.1% Triton X-100 (PBS-T) thrice, coverslips were treated with the primary antibodies at 4°C overnight before being probed with the appropriate fluorescence-conjugated secondary antibodies and 4′,6-diamidino-2-phenylindole (DAPI). Images were acquired by confocal microscopy (Carl Zeiss).

Immunohistochemistry

For tissue immunohistochemistry (IHC), it was performed using a PANO Multiplex IHC kit (PNO10223AD). According to the manufacturer's instructions, paraffin-embedded tissues were cut into 4-μm-thick sections. After rehydration, heat-induced antigen retrieval using tris-EDTA buffer, endogenous peroxidases blocking the sections were incubated with primary antibodies at 4°C overnight and with secondary antibodies at room temperature for 30 min, then it probed with the tyramide signal amplification (TSA) fluorescence and DAPI. Images were acquired by confocal microscopy (Carl Zeiss).

Detection of PD-L1 on the cell surface

After transfection with siRNA or induction with IFN-γ, RDN, or TM for the indicated time, cells were trypsinized and washed with PBS twice. The cells were then incubated with phycoerythrin-conjugated anti-human PD-L1 antibody (BioLegend, USA) for 30 min on a table rotary shaker. After incubation, the stained cells were washed twice with cold PBS and analyzed by flow cytometry. All staining steps were protected from light.

Focused in vivo CRISPR screens

B16-RFP cells were transduced with a focused library containing sgRNAs targeting the eight VPS members (nine sgRNAs per gene). Transduced cells were sorted by fluorescence-activated cell sorting (FACS) and then cultured for 6 days, then we injected those cells in either $CD8^+$ T cell–depleted mice or immune-competent mice. We ended the experiments on day 15 and collected the cancer cells. Extract the gDNA and send it for the next sequencing. The log 2-fold change (LFCs) of immune selection were calculated by the average $\log_2$-fold change (isotype/anti-CD8) of all sgRNAs targeting a given gene.

Coimmunoprecipitation

293 T cells were lentivirally transduced to express VPS18-FLAG and Rab11A for 2 days, and cells were harvested and incubated with Flag beads at 4°C overnight. Following that, beads were washed three times with lysis buffer. After boiling the beads in the sample buffer, the supernatant and elution were used for the Western blot.

For endogenous protein IP

Endogenous protein-protein interactions were detected using Universal Magnetic Co-IP Kit (Proteintech, 54002) according to the manufacturer's manual. A549 cells were harvested in lysis buffer with supplementation of protease inhibitor cocktail (Roche, #11836153001) on ice. PD-L1 antibody was mixed with cell lysates and incubated at 4°C overnight. The next day, protein A/G beads were added to the mixtures for immunoprecipitation and incubated at 4°C for 3 hours. After boiling the beads in the loading buffer, the supernatant was used for the Western blot.

T cell–mediated (PMBCs) tumor cell–killing assay

Human PBMCs were bought from NovoBiotec (#932057) were treated with a T Cell Activation/Expansion Kit (Miltenyi Biotec, #130-093-627) according to the manufacturer's protocol. We seeded both wild-type (WT) and VPS11/18 KO A549 cells into a 96-well plate at a density of 2500 cells per well and then added activated PBMC cells at a ratio of 1:10 for 6 hours. To detect apoptotic cells, all the cells were harvested with trypsin into different centrifuge tubes and incubated with allophycocyanin (APC)–conjugated anti-human CD45 antibodies (BD Biosciences) in staining buffer at 4°C for 30 min in the dark. The cells were then washed and stained with annexin V–FITC/PI to detect apoptotic cells by using flow cytometry.

T cell–mediated (Jurkat cells) tumor cell–killing assay

Human T cell–mediated tumor cell–killing assay could be conducted by the xCELLigence system (Agilent, San Diego, CA, USA).

Succinctly, 50 μl of culture medium was introduced into every well of the E-plate 16, subsequently supplemented with an additional 50 μl of medium comprising 5×10^3 H460 cells. There are three replicates included in each treatment. Following a 24-hour treatment with the specified RDN concentration, Jurkat T cells that were pretreated with PHA (1 μg/ml) for 48 hours, as described previously (*38*), were introduced at a 1:3 ratio. The xCELLigence system (Agilent) with RTCA Software was used to conduct a real-time analysis of the results.

Tumor inoculation and dissection

For tumor inoculation, 1×10^6 to 1.5×10^6 LLC-RFP cells (WT/VPS11/18 KO cells) were subcutaneously injected into the C57 mice. Tumor sizes were measured every 3 days. For tumor dissection, LLC-RFP tumors were isolated on day 18 after inoculation. Tumors were subjected to image and weight upon harvest. Liberase TM (7.7 mg/ml; Roche, #5401119001) and deoxyribonuclease I (100 mg/ml; Invitrogen, #EN0521) were then used to digest the tumor chunks. Single-cell suspensions were generated by smashing the digested tumor chunks through 70-mm strainers (BD Biosciences). Tumor cells were then subjected to flow cytometric analyses.

Tissue distribution study by MALDI-MSI

The C57BL/6 mice were divided into seven groups, with three mice in each group, in a random manner. The mice were given RDN (20 mg/kg) via the tail vein. The heart, liver, spleen, lung, kidney, and brain tissues of the mice were dissected at 2 hours, 4 hours, 8 hours, 12 hours, 24 hours, 4 days, and 6 days following administration. The mouse tissues were embedded in the inclusion agent O.C.T., and 10-μm-thick tissue slices were prepared by CryoStar NX50. All the tissues of the same mouse were prepared on the same slide. Tissue sample slides dried in a vacuum for 1 hour were subjected to matrix-assisted laser desorption ionization (MALDI) for high-resolution MSI measurements. The data were obtained in positive ion mode. Red-green-blue (RGB) images are generated via the software "MIRION," which are converted from the original file. Relative quantification of image data was performed by normalizing DHB mass spectrometry signals.

Tissue distribution study by HLPC-MS

The tissue homogenate samples were then tested by liquid-mass combined apparatus. The samples of heart, liver, spleen, lung, kidney, and brain tissues were weighed, added with 1 ml of methanol, ground for 5 min, vortexed for 5 min, centrifuged at 13,000 rpm for 10 min, filtered the supernatant with 0.22-μm filter membrane, and taken filtrate for analysis. The filtrate of liver, lung, and kidney samples was diluted 10 times before taking sample analysis. Chromatograms of analytes were collected and integrated by the software Xcalibur 3.0 Thermo. Linear regression was performed with a weighted coefficient ($1/X^2$).

Pharmacokinetic study by HLPC-MS

Three SD rats were injected with RDN (20 mg/kg) through the tail vein. Samples of blood were taken at various time points after administration, including 0 min, 5 min, 15 min, 30 min, 1 hour, 2 hours, 4 hours, 8 hours, 12 hours, 24 hours, 3 days, 4 days, and 6 days. The blood was placed in a 1.5-ml centrifuge tube humidified with heparin sodium, centrifuged at 4°C at 5000 rpm for 15 min, and the supernatant was placed at −80°C for testing. Protein was precipitated by adding 150 μl of methanol to 50 μl of plasma, vortexed and mixed for 10 min, and centrifuged at 13,000 rpm for 10 min. Subsequently, the supernatant was detected by LC-MS/MS.

Cell-based ELISA

A 96-well plate was used to plate 1×10^4 H460 cells per well, which were then cultured overnight. The cells were exposed to natural compounds for 24 hours. The cells were treated with 4% paraformaldehyde at ambient temperature for a period of 20 min. The cells were added 50 μl of 3% BSA to each well at 37°C for 1 hour. The cells were added 50 μl of PD-L1 antibody at 37°C for 2 hours. The cells were added to a second antibody labeled with horseradish peroxidase at 37°C for 0.5 hours. Then, the cells were added 100 μl of 3,3′, 5,5″-tetramethylbenzidine (TMB) substrate to each well at room temperature for 30 min. Last, the cells were added 100 μl of H_2SO_4 to stop the reaction. The microplate reader (BioTek, USA) was used to assess the OD value at 450 nm. The down-regulation level of PD-L1 was calculated.

Tumor sample digestion and flow cytometry analysis

The subcutaneous tumors were excised, digested, and made into a single-cell suspension with a Tumor Dissociation Kit (Miltenyi Biotec, Germany) according to the manufacturer's instructions. Then, the samples were passed through 70-μm cell strainers followed by a staining procedure with fluorescently labeled antibodies (anti–PD-L1, anti-CD45, anti-CD3, and anti-CD8a; BioLegend). All staining steps were protected from light and then were analyzed quantitatively by FACS (Beckman, CytoFLEX). Statistical analysis was performed using FlowJo. The detailed antibody information is included in table S4.

Animal experiments in the subcutaneous tumor-bearing model

Stable RM1/Doc, RM1/DocV18-low, RM1, and RM1V18-high cells (1×10^6) were suspended in 100 μl of normal saline and were injected into the right flanks of the mice and allowed to establish tumors. The mice tumor volumes were measured every 2 days. Tumor volume (in cubic millimeters) was calculated as $0.5 \times L \times W^2$ (L = length, W = width). For treatment with checkpoint therapy, 200 μg of an anti–CTLA-4 monoclonal antibody or isotype IgG (once every 5 days) was injected intraperitoneally into each mouse with or without RDN (20 mg/kg) or HCQ (60 mg/kg, once every 2 days). The mice were euthanized humanely at the indicated time point after tumor cells inoculation and tumors were harvested for subsequent analysis.

Animal experiments in the orthotopic lung cancer model

Sixty microliters of mixed suspension containing LLC-Luc cells (3×10^5 cells) were implanted in the lung of C57BL/6 mice to construct an in situ model of lung cancer. Then, mice were randomly divided into the model group, RDN (10 mg/kg), RDN (10 mg/kg) combined with the anti–CTLA-4 group, and the anti–CTLA-4 group (100 μg). Each group consisted of 14 mice, 6 for pharmacodynamic evaluation and 8 for survival analysis. One week after surgery, the orthotopic lung cancer model was confirmed by IVIS Spectrum. During administration, the body weight was weighed every 2 days and the growth of lung tumors was monitored with IVIS Spectrum and micro–computed tomography. At the end of the administration, the lungs, liver, spleen, and kidney of the mice were dissected. The levels

of $CD4^+$/Foxp3/$CD8^+$/PD-L1/Ki67/GzmB in the tumor microenvironment were analyzed by immunofluorescence and IHC. The lung, liver, spleen, and kidney were fixed in 4% paraformaldehyde, then the samples were captured by an inverted microscope (Olympus BX6) after hematoxylin and eosin (H&E) staining.

Animal experiments in the experimental lung metastasis model

B16-luc cells (5×10^5) were injected via the tail vein of C57BL/6 mice. Then, they were randomly divided into the model group, the RDN group (5, 10, and 20 mg/kg), RDN (5, 10, 20 mg/kg) combined with the anti–CTLA-4 group, and the anti–CTLA-4 group (200 μg) ($n = 6$). The administration began one day after vein inoculation. During the treatment, the body weight of mice was weighed every 2 days, and the metastases of pulmonary melanoma were monitored by IVIS Spectrum. The nodules of the lung were counted. The lung was fixed in 4% paraformaldehyde, then the samples were captured by an inverted microscope (Olympus BX6) after H&E staining.

Statistical analysis

The data are presented as the means ± SD and were analyzed with GraphPad Prism software (GraphPad). Student's t test or one-way analysis of variance (ANOVA) was used for comparisons among different groups. Kaplan-Meier and Cox proportional hazards analyses were used for survival analysis. All the experiments were repeated at least three times. Values of $P < 0.05$ denoted statistical significance and are indicated as $^*P \leq 0.05$, $^{**}P \leq 0.01$, $^{***}P \leq 0.001$, and $^{****}P \leq 0.0001$ in the figures.

Supplementary Materials

This PDF file includes:

Figs. S1 to S7
Tables S1 to S4

REFERENCES AND NOTES

1. Y. Wang, M. Wang, H. X. Wu, R. H. Xu, Advancing to the era of cancer immunotherapy. *Cancer Commun.* **41**, 803–829 (2021).
2. M. Reck, D. Rodríguez-Abreu, A. G. Robinson, R. Hui, T. Csőszi, A. Fülöp, M. Gottfried, N. Peled, A. Tafreshi, S. Cuffe, Pembrolizumab versus chemotherapy for PD-L1–positive non–small-cell lung cancer. *N. Engl. J. Med.* **375**, 1823–1833 (2016).
3. J. R. Brahmer, S. S. Tykodi, L. Q. Chow, W.-J. Hwu, S. L. Topalian, P. Hwu, C. G. Drake, L. H. Camacho, J. Kauh, K. Odunsi, Safety and activity of anti–PD-L1 antibody in patients with advanced cancer. *N. Engl. J. Med.* **366**, 2455–2465 (2012).
4. F. S. Hodi, S. J. O'day, D. F. McDermott, R. W. Weber, J. A. Sosman, J. B. Haanen, R. Gonzalez, C. Robert, D. Schadendorf, J. C. Hassel, Improved survival with ipilimumab in patients with metastatic melanoma. *N. Engl. J. Med.* **363**, 711–723 (2010).
5. R. Offringa, L. Kötzner, B. Huck, K. Urbahns, The expanding role for small molecules in immuno-oncology. *Nat. Rev. Drug Discov.* **21**, 821–840 (2022).
6. P. Sharma, S. Hu-Lieskovan, J. A. Wargo, A. Ribas, Primary, adaptive, and acquired resistance to cancer immunotherapy. *Cell* **168**, 707–723 (2017).
7. T. K. Kim, E. N. Vandsemb, R. S. Herbst, L. Chen, Adaptive immune resistance at the tumour site: Mechanisms and therapeutic opportunities. *Nat. Rev. Drug Discov.* **21**, 529–540 (2022).
8. L. Gandhi, D. Rodríguez-Abreu, S. Gadgeel, E. Esteban, E. Felip, F. De Angelis, M. Domine, P. Clingan, M. J. Hochmair, S. F. Powell, Pembrolizumab plus chemotherapy in metastatic non–small-cell lung cancer. *N. Engl. J. Med.* **378**, 2078–2092 (2018).
9. J.-H. Cha, L.-C. Chan, C.-W. Li, J. L. Hsu, M.-C. Hung, Mechanisms controlling PD-L1 expression in cancer. *Mol. Cell* **76**, 359–370 (2019).
10. M. L. Burr, C. E. Sparbier, Y.-C. Chan, J. C. Williamson, K. Woods, P. A. Beavis, E. Y. Lam, M. A. Henderson, C. C. Bell, S. Stolzenburg, CMTM6 maintains the expression of PD-L1 and regulates anti-tumour immunity. *Nature* **549**, 101–105 (2017).
11. H. Wang, H. Yao, C. Li, H. Shi, J. Lan, Z. Li, Y. Zhang, L. Liang, J.-Y. Fang, J. Xu, HIP1R targets PD-L1 to lysosomal degradation to alter T cell–mediated cytotoxicity. *Nat. Chem. Biol.* **15**, 42–50 (2019).
12. J.-H. Cha, W.-H. Yang, W. Xia, Y. Wei, L.-C. Chan, S.-O. Lim, C.-W. Li, T. Kim, S.-S. Chang, H.-H. Lee, Metformin promotes antitumor immunity via endoplasmic-reticulum-associated degradation of PD-L1. *Mol. Cell* **71**, 606–620.e7 (2018).
13. Y. Ren, Y. Qian, L. Ai, Y. Xie, Y. Gao, Z. Zhuang, J. Chen, Y.-X. Chen, J.-Y. Fang, TRAPPC4 regulates the intracellular trafficking of PD-L1 and antitumor immunity. *Nat. Commun.* **12**, 5405 (2021).
14. C. Bröcker, A. Kuhlee, C. Gatsogiannis, H. J. K. Balderhaar, C. Hönscher, S. Engelbrecht-Vandré, C. Ungermann, S. Raunser, Molecular architecture of the multisubunit homotypic fusion and vacuole protein sorting (HOPS) tethering complex. *Proc. Natl. Acad. Sci. U.S.A.* **109**, 1991–1996 (2012).
15. S. C. Graham, L. Wartosch, S. R. Gray, E. J. Scourfield, J. E. Deane, J. P. Luzio, D. J. Owen, Structural basis of Vps33A recruitment to the human HOPS complex by Vps16. *Proc. Natl. Acad. Sci. U.S.A.* **110**, 13345–13350 (2013).
16. J. van der Beek, C. Jonker, R. van der Welle, N. Liv, J. Klumperman, CORVET, CHEVI and HOPS–multisubunit tethers of the endo-lysosomal system in health and disease. *J. Cell Sci.* **132**, jcs189134 (2019).
17. E. Monfrini, F. Cogiamanian, S. Salani, L. Straniero, G. Fagiolari, M. Garbellini, E. Carsana, L. Borellini, F. Biella, M. Moggio, A novel homozygous VPS11 variant may cause generalized dystonia. *Ann. Neurol.* **89**, 834–839 (2021).
18. C. Peng, J. Ye, S. Yan, S. Kong, Y. Shen, C. Li, Q. Li, Y. Zheng, K. Deng, T. Xu, Ablation of Vacuole Protein Sorting 18 (Vps18) gene leads to neurodegeneration and impaired neuronal migration by disrupting multiple vesicle transport pathways to lysosomes. *J. Biol. Chem.* **287**, 32861–32873 (2012).
19. S.-O. Lim, C.-W. Li, W. Xia, J.-H. Cha, L.-C. Chan, Y. Wu, S.-S. Chang, W.-C. Lin, J.-M. Hsu, Y.-H. Hsu, Deubiquitination and stabilization of PD-L1 by CSN5. *Cancer Cell* **30**, 925–939 (2016).
20. G. Segala, M. A. Bennesch, N. M. Ghahhari, D. P. Pandey, P. C. Echeverria, F. Karch, R. K. Maeda, D. Picard, Vps11 and Vps18 of Vps-C membrane traffic complexes are E3 ubiquitin ligases and fine-tune signalling. *Nat. Commun.* **10**, 1833 (2019).
21. H. Niu, L. Qian, Y. Luo, F. Wang, H. Zheng, Y. Gao, H. Wang, X. Hu, H. Yuan, H. Lou, Targeting of VPS18 by the lysosomotropic agent RDN reverses TFE3-mediated drug resistance. *Signal Transduct. Target. Ther.* **6**, 224 (2021).
22. Q. Gou, C. Dong, H. Xu, B. Khan, J. Jin, Q. Liu, J. Shi, Y. Hou, PD-L1 degradation pathway and immunotherapy for cancer. *Cell Death Dis.* **11**, 955 (2020).
23. H. Behrmann, A. Lürick, A. Kuhlee, H. K. Balderhaar, C. Bröcker, D. Kümmel, S. Engelbrecht-Vandré, U. Gohlke, S. Raunser, U. Heinemann, Structural identification of the Vps18 β-propeller reveals a critical role in the HOPS complex stability and function. *J. Biol. Chem.* **289**, 33503–33512 (2014).
24. M. R. Hunter, E. J. Scourfield, E. Emmott, S. C. Graham, VPS18 recruits VPS41 to the human HOPS complex via a RING–RING interaction. *Biochem. J.* **474**, 3615–3626 (2017).
25. J. S. Bonifacino, R. Rojas, Retrograde transport from endosomes to the trans-Golgi network. *Nat. Rev. Mol. Cell Biol.* **7**, 568–579 (2006).
26. C.-W. Li, S.-O. Lim, W. Xia, H.-H. Lee, L.-C. Chan, C.-W. Kuo, K.-H. Khoo, S.-S. Chang, J.-H. Cha, T. Kim, Glycosylation and stabilization of programmed death ligand-1 suppresses T-cell activity. *Nat. Commun.* **7**, 12632 (2016).
27. J. Breitling, M. Aebi, N-linked protein glycosylation in the endoplasmic reticulum. *Cold Spring Harb. Perspect. Biol.* **5**, a013359 (2013).
28. C.-W. Li, S.-O. Lim, E. M. Chung, Y.-S. Kim, A. H. Park, J. Yao, J.-H. Cha, W. Xia, L.-C. Chan, T. Kim, Eradication of triple-negative breast cancer cells by targeting glycosylated PD-L1. *Cancer Cell* **33**, 187–201.e10 (2018).
29. N. Abdullah, M. Beg, D. Soares, J. S. Dittman, T. E. McGraw, Downregulation of a GPCR by β-Arrestin2-mediated switch from an endosomal to a TGN recycling pathway. *Cell Rep.* **17**, 2966–2978 (2016).
30. G. Zhang, X. Tang, L. Liang, W. Zhang, D. Li, X. Li, D. Zhao, Y. Zheng, Y. Chen, B. Hao, DNA and RNA sequencing identified a novel oncogene VPS35 in liver hepatocellular carcinoma. *Oncogene* **39**, 3229–3244 (2020).
31. M. N. Seaman, The retromer complex: From genesis to revelations. *Trends Biochem. Sci.* **46**, 608–620 (2021).
32. M. A. De Matteis, A. Luini, Exiting the Golgi complex. *Nat. Rev. Mol. Cell Biol.* **9**, 273–284 (2008).
33. A. Lin, C. J. Giuliano, A. Palladino, K. M. John, C. Abramowicz, M. L. Yuan, E. L. Sausville, D. A. Lukow, L. Liu, A. R. Chait, Off-target toxicity is a common mechanism of action of cancer drugs undergoing clinical trials. *Sci. Transl. Med.* **11**, eaaw8412 (2019).
34. R. Giavazzi, A. Decio, Syngeneic murine metastasis models: B16 melanoma. *Methods Mol. Biol.* **1070**, 131–140 (2014).
35. A. V. Kornepati, R. K. Vadlamudi, T. J. Curiel, Programmed death ligand 1 signals in cancer cells. *Nat. Rev. Cancer* **22**, 174–189 (2022).
36. A. T. Ritter, G. Shtengel, C. S. Xu, A. Weigel, D. P. Hoffman, M. Freeman, N. Iyer, N. Alivodej, D. Ackerman, I. Voskoboinik, ESCRT-mediated membrane repair protects tumor-derived cells against T cell attack. *Science* **376**, 377–382 (2022).
37. D. Bansal, M. A. Reimers, E. M. Knoche, R. K. Pachynski, Immunotherapy and immunotherapy combinations in metastatic castration-resistant prostate cancer. *Cancer* **13**, 334 (2021).

38. G. Gulden, B. Sert, T. Teymur, Y. Ay, N. N. Tiryaki, A. K. Mishra, E. Ovali, N. Tarhan, C. Tastan, CAR-T cells with phytohemagglutinin (PHA) provide anti-cancer capacity with better proliferation, rejuvenated effector memory, and reduced exhausted t cell frequencies. *Vaccine* **11**, 313 (2023).

Acknowledgments: We thank Y. Kawaoka (University of Tokyo) for providing the VPS18 plasmids. **Funding:** This work was supported by the National Natural Science Foundation of China (82173839, 82293682, 32100989, 82002942, and 82204404), Natural Science Foundation of Shandong Province (ZR2021QC074 and ZR2020QH175), Natural Science Foundation for Excellent Young Scholars of Shandong Province in China (2022HWYQ-033), GXRC Program of Ji-Nan Science & Technology Bureau (2021GXRC102), National Key R&D Program of China (no. 2019YFA0905701), Major Basic Research Program of the Shandong Provincial Natural Science Foundation of China (ZR2019ZD26), ECCM Program of Clinical Research Center of Shandong University (2021SDUCRC003), and Special Funding for Taishan Scholar Program (tstp20221159 and tsqn202306070). **Author contributions:** Supervision and experimental design: H.Y. and H.L. Writing—original draft: T.D. and H.N. Most of the experimental operations: H.N., Z.C., and T.D. Clinical specimens: C.Z. and G.S. Western blot and data analysis: Y.G., Q.L., W.Z., and C.L. In vivo experiment assistance: X.Z., Y.L., M.J., and Y.S. Chemical synthesis: B.S. IMS experiment assistance: J.Z. and C.W. **Competing interests:** The authors declare that they have no competing interests. **Data and materials availability:** All data needed to evaluate the conclusions in the paper are present in the paper and/or the Supplementary Materials.

Submitted 27 March 2024
Accepted 12 September 2024
Published 16 October 2024
10.1126/sciadv.adp4917